The Astrophysical Journal, 840:15 (17pp), 2017 May 1 https://doi.org/10.3847/1538-4357/aa6c5b

The IRX–β Relation: Insights from Simulations

Mohammadtaher Safarzadeh[1], Christopher C. Hayward[2,3,4], and Henry C. Ferguson[5]
[1] Johns Hopkins University, Department of Physics and Astronomy, 366 Bloomberg Center, 3400 N. Charles Street, Baltimore, MD 21218, USA; mts@pha.jhu.edu
[2] Center for Computational Astrophysics, Flatiron Institute, 162 Fifth Avenue, New York, NY 10010, USA; chayward@simonsfoundation.org
[3] TAPIR 350-17, California Institute of Technology, 1200 E. California Boulevard, Pasadena, CA 91125, USA
[4] Harvard–Smithsonian Center for Astrophysics, 60 Garden Street, Cambridge, MA 02138, USA
[5] Space Telescope Science Institute, 3700 San Martin Boulevard, Baltimore, MD 21218, USA; ferguson@stsci.edu
Received 2016 April 25; revised 2017 April 3; accepted 2017 April 6; published 2017 April 28

Abstract

We study the relationship between the UV continuum slope and infrared excess (IRX $\equiv L_{\rm IR}/L_{\rm FUV}$) predicted by performing dust radiative transfer on a suite of hydrodynamical simulations of galaxies. Our suite includes both isolated disk galaxies and mergers intended to be representative of galaxies at both $z \sim 0$ and $z \sim 2$–3. Our low-redshift systems often populate a region around the locally calibrated Meurer et al. relation but move above the relation during merger-induced starbursts. Our high-redshift systems are blue and IR luminous and therefore lie above the Meurer et al. relation. The value of β strongly depends on the dust type used in the RT simulation: Milky-Way-type dust leads to significantly more negative (bluer) slopes compared with Small-Magellanic-Cloud-type dust. The effect on β due to variations in the dust composition with galaxy properties or redshift is the dominant model uncertainty. The dispersion in β is anticorrelated with specific star formation rate (sSFR) and tends to be higher for the $z \sim 2$–3 simulations. In the actively star-forming $z \sim 2$–3 simulated galaxies, dust attenuation dominates the dispersion in β, whereas in the $z \sim 0$ simulations, the contributions of star formation history (SFH) variations and dust are similar. For low-sSFR systems at both redshifts, SFH variations dominate the dispersion. Finally, the simulated $z \sim 2$–3 isolated disks and mergers both occupy a region in the IRX–β plane consistent with observed $z \sim 2$–3 dusty star-forming galaxies (DSFGs). Thus, contrary to some claims in the literature, the blue colors of high-z DSFGs do not imply that they are short-lived starbursts.

Key words: dust, extinction – infrared: galaxies – radiative transfer – ultraviolet: galaxies

1. Introduction

Dust plays a key role in many areas of astrophysics. In galaxies, it obscures emission from stars and active galactic nuclei (AGNs), thereby making it more difficult to infer the properties of these objects, such as stellar ages. Various approaches are used to correct for the effects of dust attenuation; one popular approach is to use the so-called "IRX–β" relation. Here, β refers to the ultraviolet (UV) continuum slope, which is defined by assuming that the UV regime of galaxy spectral energy distributions (SEDs) can be described by a power law, $f_\lambda \propto \lambda^\beta$ (e.g., Calzetti et al. 1994; Meurer et al. 1999, hereafter M99). Dust reddening and older stellar populations both cause the UV continuum to be steeper and thus β to be more positive. IRX denotes the "infrared excess" and is defined as IRX $\equiv L_{\rm IR}/L_{\rm FUV}$, where $L_{\rm IR}$ and $L_{\rm FUV}$ are the total infrared (IR) and far-UV luminosities, respectively. M99 demonstrated that local starburst galaxies exhibit a relatively tight, monotonic relation between IRX and β.

Recent recalibrations of the IRX–β relation prefer lower values of IRX for the same UV slope compared with the M99 relation (Overzier et al. 2011; Takeuchi et al. 2012; Casey et al. 2014; Álvarez-Márquez et al. 2016). It has been found that massive galaxies at high redshifts have similar IRX values to their low-redshift counterparts but with bluer UV slopes (Álvarez-Márquez et al. 2016), which implies that using the locally calibrated IRX–β relation would cause one to underestimate the star formation rates (SFRs) of high-mass Lyman break galaxies (LBGs). Therefore, we should reconsider the similarity of the LBGs (Steidel et al. 1996) at $z \sim 2$ to local starburst galaxies based on high-redshift LBGs falling onto the M99 relation (Reddy et al. 2012).

Due to the sensitivity and confusion limits (Safarzadeh et al. 2015) of current IR surveys, for many UV-selected galaxies, the IR luminosity is unknown; thus, inferring the dust obscuration from the UV slope β is highly desirable if one wishes to constrain the total star formation history (SFH) of the universe (e.g., Bouwens et al. 2009, 2012, 2014; Dunlop et al. 2012; Finkelstein et al. 2012). For galaxies for which the M99relation holds, the observed slope can in principle be used to infer the amount of UV light that has been obscured by dust, and thus one can obtain the intrinsic UV flux and total SFR from UV observations alone.[6]

If observations and/or simulations indicate that there is significant dispersion in IRX for a fixed value of β, then it would be useful to determine whether there are other UV–optical observable properties of a galaxy that could be used to predict its location in the IRX–β plane. It is known that (ultra)luminous infrared galaxies [(U)LIRGs], alternatively referred to as dusty star-forming galaxies (DSFGs), do not obey any well-defined IRX–β relation (Bell et al. 2002; Goldader et al. 2002; Howell et al. 2010; Casey et al. 2014). Furthermore, recent studies have revealed more scatter than the original M99 work, even if (U)LIRGs are excluded. Assuming an exponentially declining SFH, Kong et al. (2004) suggest that

[6] However, it is important to note that stellar populations older than 10–100 Myr can "contaminate"—and sometimes even dominate—both the intrinsic UV and observed IR emission of galaxies (e.g., Salim et al. 2009; Kelson & Holden 2010; Groves et al. 2012; Leroy et al. 2012; Smith et al. 2012; Fumagalli et al. 2013; Hayward et al. 2014; Utomo et al. 2014). We will not discuss this issue further in this work, but this caveat should be kept in mind.

the dispersion in IRX–β can be explained by the ratio of the recent SFR to the SFR averaged over a longer timescale (a proxy for the SFH). Kong et al. (2004) show that the distance of galaxies from the M99 relation exhibits no correlation with the dust-sensitive Hα/Hβ ratio (i.e., the Balmer decrement), thus suggesting that dust attenuation is not responsible for the dispersion in the relation. In contrast, Cortese et al. (2006) conclude that different dust geometries can explain the observed dispersion, but this conclusion may be affected by calibration issues (Casey et al. 2014). We discuss our results regarding the source of dispersion in Section 5.

The goal of this paper is to understand how galaxies might be *expected* to evolve in the IRX–β plane given reasonable geometries, SFHs, merger parameters, etc., and accounting for viewing-angle-related effects. We wish to address questions such as the following: How much of the dispersion in β at fixed IRX is due to viewing angle? How much of the dispersion is due to physical differences such as SFHs and dust geometries? How do galaxy mergers evolve in the IRX–β plane? Are high-redshift DSFGs predominantly merger systems or isolated disks?

To address the above questions, we analyze a set of 51 idealized (i.e., noncosmological) galaxy simulations, including both mergers and isolated disks, that are intended to be representative of both low-redshift ($z \sim 0$) and high-redshift ($z \sim 2$–3) galaxies. In post-processing, we perform dust radiative transfer on the simulated galaxies at various times to predict their UV–millimeter SEDs. This enables us to *forward-model* the positions of the simulated galaxies in the IRX–β plane. These or similar simulations have been shown to be in good agreement with the SEDs/colors of diverse classes of real galaxies, such as local normal star-forming galaxies (Jonsson et al. 2010), (U)LIRGs (Younger et al. 2009; Jonsson et al. 2010; Lanz et al. 2014, hereafter L14), high-redshift DSFGs (Narayanan et al. 2010; Hayward et al. 2011, 2012), obscured AGNs (Snyder et al. 2013), and post-starburst galaxies (Snyder et al. 2011). We analyzed the same set of simulations in Safarzadeh et al. (2016), where we showed that the dispersion in the FIR SEDs of our simulated galaxies is determined primarily by the luminosity absorbed by dust and dust mass (i.e., dust geometry is subdominant).

The remainder of this paper is organized as follows: In Section 2, we summarize the details of the simulated galaxy SED data set used in this work. Section 3 discusses how the SFR, observed and intrinsic UV continuum slopes, and IRX values of some representative isolated disk and galaxy merger simulations evolve in the IRX–β plane. Section 4 demonstrates how the results depend on the dust model assumed in the radiative transfer calculations. In Section 5, we investigate the dispersion in the IRX–β relation. Section 7 discusses the location of DSFGs in the IRX–β plane. In Section 8, we compare our results with previous work. Section 9 presents some implications for interpreting observations. Section 10 discusses the limitations of this work and provides suggestions for future work, and Section 11 summarizes our conclusions. In the appendices, we demonstrate that our results are converged with respect to the resolution of the hydrodynamical simulations, discuss the uncertainties associated with the input SED templates, and model for subresolution dust structure employed in the radiative transfer calculations (both of which do not significantly affect our results).

2. Simulated Galaxy SED Data Set

Our low-redshift simulation data set was presented in L14. The four progenitor disk galaxies span a stellar (baryonic) mass range of 6×10^8–$4 \times 10^{10}\,M_\odot$ (10^9–$5 \times 10^{10}\,M_\odot$), and their properties were selected to represent typical star-forming galaxies in the local universe (Cox et al. 2008). Each of the four progenitors—together with the 10 different possible combinations of them as merger systems—was simulated for a single non-"special" orbital configuration for multiple gigayears (see L14 for details). The total data set contains ∼6000 SEDs.

The details of the second set of SEDs of simulated isolated disk and merging galaxies are presented in Hayward et al. (2013b, hereafter H13). For this data set, the structural properties of the progenitor disk galaxies were scaled to $z = 3$ following Robertson et al. (2006), with the initial gas fractions of the disks (0.6–0.8) being significantly larger than those of the $z \sim 0$ simulations. Because the original purpose of this suite of simulations was to model $z \sim 2$–3 DSFGs, the progenitor disks span a relatively narrow baryonic mass range of $\sim(1$–$4) \times 10^{11}\,M_\odot$, but a variety of merger orbits and mass ratios are included. This data set contains 37 hydrodynamical simulations, from which ∼46,000 SEDs were calculated.

The full methodology is described in the aforementioned works and references therein, so we will only summarize it here. First, idealized isolated (i.e., noncosmological) galaxy models were created following the method described in Springel et al. (2005). Each initial disk galaxy is composed of a dark matter halo, stellar and gaseous disks, and a supermassive black hole (BH); for the $z \sim 0$ simulations only, a stellar bulge is also included. Then, the isolated galaxies and binary mergers of these galaxies were simulated using a heavily modified version of the GADGET-2 *N*-body/smoothed particle hydrodynamics (SPH) code (Springel 2005).[7]

The simulations include the effects of gravity, hydrodynamical interactions, and radiative heating and cooling.[8] Star formation and stellar feedback are incorporated via the two-phase subresolution interstellar medium (ISM) model of Springel & Hernquist (2003), and BH accretion and AGN feedback are treated following Springel et al. (2005). Each gas particle is enriched with metals according to its associated SFR, assuming a yield of 0.02. Instantaneous recycling is assumed.

The UV–millimeter SEDs of the simulated galaxies are forward-modeled by post-processing the outputs of the 3D hydrodynamical simulations at various times with the dust radiative transfer code SUNRISE (Jonsson 2006; Jonsson et al. 2010). For a given snapshot, the SUNRISE calculation proceeds as follows: the stellar and BH particles in the GADGET-2 simulation, which are the sources of radiation, are assigned source SEDs according to their properties (age and metallicity for the star particles and luminosity for the BH particles). The metal distribution from the simulation is projected onto an octree grid in order to calculate the dust optical depths. We use a fixed dust-to-metal ratio of 0.4 (e.g., Dwek 1998; James et al. 2002). The Milky Way (MW) $R_V = 3.1$ dust model of Draine & Li (2007) is

[7] Hayward et al. (2014) demonstrated that the results of such simulations are insensitive to the inaccuracies inherent in the traditional density–entropy formulation of SPH, so the numerical scheme employed does not represent a significant source of error.

[8] The gravitational softening lengths for baryonic particles are ∼100–150 pc, and those of the dark matter particles are 2–4 times greater (see H13 and L14 for details). We have confirmed that our results are converged with respect to the resolution of the hydrodynamical simulations (Appendix A; see also Martínez-Galarza et al. 2016).

Table 1
Properties of the Progenitor Disk Galaxies

Name	Redshift	$M_{*,\mathrm{init}}$ ($10^{10}\ M_\odot$)	$M_{\mathrm{gas,init}}$ ($10^{10}\ M_\odot$)	M_{200} ($10^{12}\ M_\odot$)	$M_{\mathrm{bulge,init}}$ ($10^{10}\ M_\odot$)	R_d (kpc)
M0	0	0.061	0.035	0.05	0.002	1.12
M1	0	0.38	0.14	0.20	0.3	1.48
M2	0	1.18	0.33	0.51	1.5	1.91
M3	0	4.22	0.8	1.16	8.9	2.85
b4	3	0.070	2.9	0.86	0	2.42
b5	3	2.0	8.0	2.4	0	2.85
b5.5	3	3.9	16	4.7	0	3.7
b6	3	7.6	31	9.1	0	4.7

used except for the runs with Small Magellanic Cloud (SMC) type dust described in Section 4. After the source and dust properties are specified, radiation transfer is performed using the Monte Carlo method to calculate the effects of dust absorption, scattering, and reemission. For each snapshot, this process yields spatially resolved UV–millimeter SEDs of the simulated galaxy/merger viewed from seven viewing angles.

Most SUNRISE parameters were set to the fiducial values determined by Jonsson et al. (2010), who compared various flux ratios spanning the UV through submillimeter of simulated isolated disk galaxies predicted using SUNRISE with those of real galaxies from the SINGS (Kennicutt et al. 2003; Dale et al. 2007) sample, generally finding good agreement. The SEDs of simulated galaxy mergers predicted using SUNRISE with the same parameters agree well with those of local interacting galaxies (L14) and high-redshift 24 μm-selected starbursts and AGNs (Roebuck et al. 2016). The sole difference in terms of SUNRISE assumptions between the simulations used in this work and those of Jonsson et al. (2010) is that in our $z = 3$ simulation suite, we set the photodissociation region (PDR) covering fraction of the Groves et al. (2008) model to 0 and employed the "multiphase-off" treatment of the ISM, in which the total dust content in the simulations, rather than just that implicit in the diffuse phase of the Springel & Hernquist (2003) subresolution ISM model, is considered when performing the radiative transfer. The motivation for this choice is discussed in Hayward et al. (2011), and we provide additional details in Appendices B and C.

Despite employing the parameter choices motivated by the aforementioned works, to ensure that the results presented in this work are robust (at least given the inherent limitations of the methods employed, which are discussed in detail in Section 10), we tested whether varying multiple potentially important assumptions in the radiative transfer calculations affected our results. Of the various parameters and assumptions investigated, we found that only the assumed dust composition had a significant effect on our results (i.e., the evolution in the IRX–β plane); this is discussed in detail in Section 4. Changing other potentially relevant assumptions typically caused the resulting β value to differ by $\sim$0.2 or less, and IRX was generally negligibly affected; see Appendices B and C for details.

In Table 1, we summarize the properties of the progenitors of merger systems that are studied here.

3. Evolution of the Simulated Galaxies in the IRX–β Plane

We will now discuss how the simulated galaxies evolve in the IRX–β plane. We present the results for two (one $z \sim 0$ and one $z \sim 2$–3) representative isolated disk galaxy simulations in Section 3.1, and two representative merger simulations are discussed in Section 3.2.

3.1. Isolated Disks

Our simulation suite contains eight isolated disk simulations, four of which are representative of $z \sim 0$ galaxies and four of which represent $z \sim 2$–3 galaxies. The details of these simulations are presented in L14 and H13, respectively.

The top panel of Figure 1 shows the time evolution of both the attenuated and intrinsic UV slopes, IRX and log SFR for one of the simulated $z \sim 0$ isolated disks, the M3 simulation of L14.[9] After an initial transient owing to the initial conditions being slightly out of equilibrium, the SFR (cyan line in the top panel) smoothly declines as the gas is depleted.[10] The UV slope measured from the attenuated SEDs is shown in red. It varies rapidly on a timescale of $\sim$100 Myr, ranging from ~ -2 to ~ -1.5, and there seems to be no long-timescale trend. The pink shaded region shows the dispersion due to the viewing angle, which is calculated as the difference between the 84th and 16th percentiles of the distribution divided by two (for a Gaussian distribution, this is equivalent to 1σ). For this particular simulation, the dispersion due to viewing angle is clearly less than that due to the time evolution of the galaxy. The UV continuum slope measured from the intrinsic (i.e., unattenuated) SEDs is shown with a thinner red line, which is below the thicker red line at all times. Both of these lines are plotted on the same scale, and the values can be read from the red axis on the right side of the figure. The differences between the observed and intrinsic UV slopes are modest, which suggests that dust attenuation does not significantly alter this simulated galaxy's UV slope. The measured IRX is indicated by the green line, and the dispersion with viewing angle is denoted by the yellow shaded region. The IRX axis values are specified by the green numbers on the left side of the figure. The IRX value is high ($\sim$10) in the early stages of the simulation, when the galaxy is still gas-rich. As the gas reservoir is depleted and dust is locked into stars, thus

[9] We measure the observed (intrinsic) UV continuum slope from the dust-attenuated (unattenuated) SED by least-squares-fitting a functional form of $f_\lambda \propto \lambda^\beta$ to the SED in the rest-frame wavelength range of 1400 Å $< \lambda <$ 2300 Å. We also measured the UV slope by convolving the rest-frame SEDs with the *GALEX* far-UV (FUV) and near-UV (NUV) filter response curves, and we obtained slopes indistinguishable from those obtained by fitting the SEDs in the rest-frame wavelength range of 1400–2300 Å. The FUV luminosity is measured from the attenuated SEDs at rest frame $\lambda = 1600$ Å, i.e., $L_\mathrm{FUV} = \lambda L_\lambda$ at $\lambda = 1600$ Å. The FIR luminosity (L_FIR) is defined by integrating the SED from 8 to 1000 μm. We then calculate IRX $\equiv L_\mathrm{FIR}/L_\mathrm{FUV}$.

[10] Because these are idealized, noncosmological simulations, no cosmological gas accretion is included.

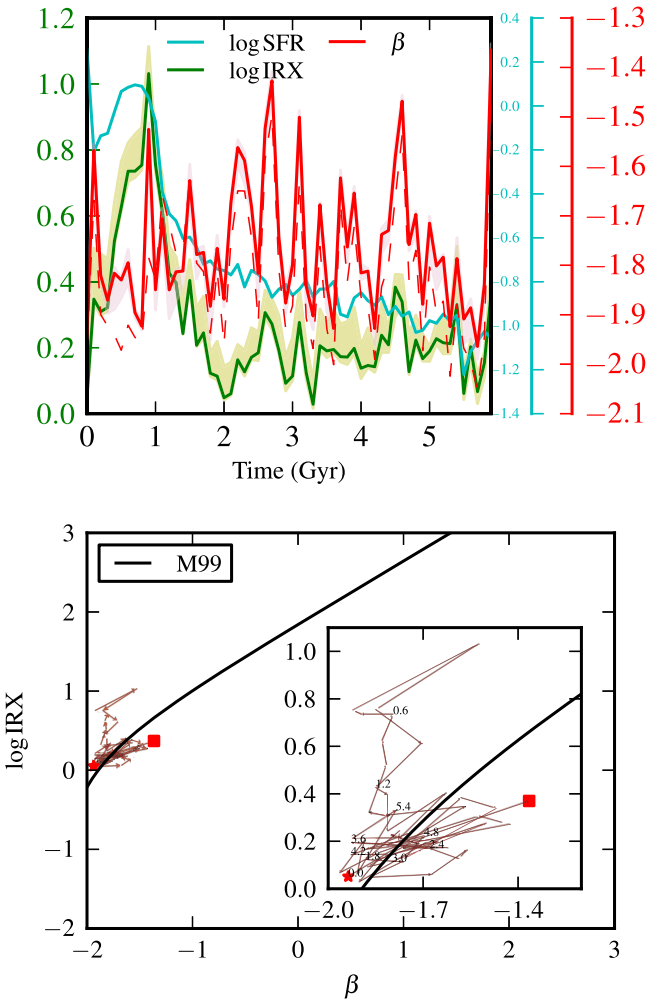

Figure 1. Results for a simulated $z \sim 0$ isolated disk galaxy, the M3 simulation of L14. Top: time evolution of log (SFR/$M_\odot$ yr^{-1}) (cyan), the observed and intrinsic (i.e., unattenuated) UV slopes β (thick solid and thin dashed red lines, respectively), and log IRX $\equiv \log(L_{\rm FIR}/L_{\rm UV})$ (green line). The observed β and IRX values depend on viewing angle; the lines correspond to the average taken over the seven viewing angles, and the shaded pink and yellow regions show the dispersion in the observed β and IRX values, respectively, over the different viewing angles (see text for details). The log IRX axis labels are provided on the left side of the figure, and the β and log SFR values are provided on the right in red and cyan text, respectively. Bottom: evolution of the simulated galaxy in the IRX–β plane. This panel utilizes axis ranges that will be used for all IRX–β plots in this work (see text for details); consequently, the data are concentrated in a small section of the plot. The inset shows a zoomed-in view of this region. The solid line shows the M99 relation. The red star indicates the initial time snapshot of the simulation, and the red square marks the final snapshot. The arrows connect individual snapshots (which are separated by 100 Myr), and the time elapsed in Gyr is labeled for a small subset of the snapshots. At all times, this simulated disk galaxy lies near the M99 relation; the "spur" above the relation corresponds to early in the simulation (first ∼1 Gyr), when the galaxy is the most gas-rich, highly star forming, and dust obscured.

decreasing the amount of dust attenuation, IRX becomes of order unity.

The bottom panel of Figure 1 shows the time evolution of this simulation in the IRX–β plane. The main figure uses the axis ranges that will be used in all IRX–β plots shown in this work.[11]

[11] The ranges were set based on the IRX–β region spanned by real galaxies (e.g., Takeuchi et al. 2012; Casey et al. 2014). Use of common axes enables the reader to more easily compare the amount of evolution exhibited by the different simulations and the magnitude of the differences that result from the choice of dust model, for example.

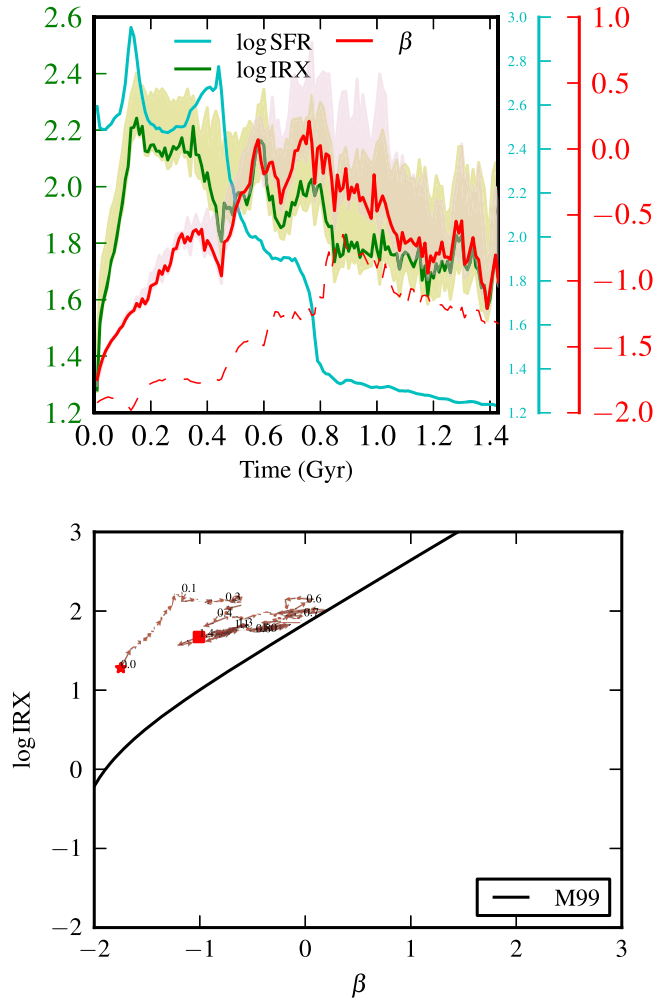

Figure 2. Time evolution (top) and IRX–β (bottom) plots shown in Figure 1 but for a simulated $z \sim 2$–3 isolated disk, b6 from H13. The difference between the UV slopes of the attenuated (thick solid red line) and unattenuated (thin dashed red line) SEDs is more pronounced compared with the $z \sim 0$ isolated disk shown in Figure 1. The simulated $z \sim 2$–3 isolated disk galaxy tends to lie above the M99 relation.

The inset shows a zoomed-in view of the region traversed by the galaxy. The initial snapshot of the simulation is marked by the red star, and the final snapshot is indicated by the red square. The arrows connect one snapshot to the next, tracing the galaxy in time. The thick black line is the M99 relation. As the simulation evolves, the galaxy wanders around the M99 relation and crosses it many times, but it is typically close to the relation. The "spur" above the relation corresponds to the first ∼1 Gyr, when the galaxy is still gas-rich and dust obscured, as indicated by the high IRX values shown in the top panel.

Figure 2 shows the results for one of the $z \sim 2$–3 isolated disk simulations from H13, b6. This simulation differs from that shown in Figure 1 in a few important aspects: First, its baryonic mass is 4×10^{11} $M_\odot$, whereas that of the $z \sim 0$ simulation is 5×10^{10} $M_\odot$. The $z \sim 2$–3 disk galaxy has an initial gas fraction $f_g \equiv M_{\rm gas}/(M_{\rm stars} + M_{\rm gas}) = 0.8$, whereas the $z \sim 0$ disk has $f_g = 0.16$. The simulated $z \sim 0$ disk galaxy contains a bulge, which acts to stabilize the gas disk, whereas the $z \sim 2$–3 disk galaxy does not. The star particles in the initial conditions are assigned ages and metallicities appropriate for the assumed redshift; thus, a significant fraction of the initial stellar mass of the $z \sim 2$–3 disk is composed of young

and intermediate-age stars, whereas the stellar-mass $z \sim 0$ disk is always dominated by old stellar populations. Finally, the structural properties of this galaxy (e.g., dark matter halo and disk scale length) have been scaled to $z = 3$ (see H13 for details). The above differences imply that the $z \sim 2$–3 disk has a much higher gas surface density, and thus SFR surface density, than does the $z \sim 0$ disk.

The top panel of Figure 2 shows that the time evolutions of the SFR and IRX are qualitatively similar to those of the $z \sim 0$ galaxy discussed above, although both the SFR and IRX values are considerably greater than for the $z \sim 0$ disk owing to the much higher gas surface density (and thus attenuation) in the $z \sim 2$–3 simulation. In contrast with the $z \sim 0$ simulation, there is a long-term trend in β. The value of β tends to increase (i.e., the SED becomes redder) until ∼0.7 Gyr, after which it decreases (the SED becomes bluer). The reason for this qualitatively different behavior is that in the $z \sim 2$–3 simulations, a significant fraction of the preexisting stars have ages of a few hundred megayears and can thus contribute significantly to the UV emission. As these stars age, the UV slope becomes redder. The IRX values start a gradual decline after 700 Myr, while the SED becomes bluer. Another significant difference is that for the $z \sim 2$–3 simulation, the difference between the UV slopes of the attenuated (thick red line) and intrinsic (red dashed line) SEDs is considerable. The attenuated and intrinsic β values can differ by as much as ∼2, which indicates that dust reddening significantly affects the UV slope measured for this galaxy, unlike for the $z \sim 0$ galaxy. Relatedly, the viewing-angle-dependent dispersion in β and IRX (the pink and yellow shaded regions, respectively) is significant, again in contrast with the $z \sim 0$ disk galaxy simulation discussed above. It is worth noting that the difference between the observed and intrinsic β values varies with time, and it becomes less as the gas is depleted and the galaxy's ISM becomes less opaque to UV photons as dust is locked into stars.

The bottom panel of Figure 2 summarizes the evolution in the IRX–β plane. The galaxy tends to lie above the M99 relation, and it comes close to the relation only at around the time when it experiences a sharp decline in SFR at ∼0.7 Gyr. For such a galaxy, using the measured UV slope and the M99 relation to correct for dust would cause one to significantly underpredict the IR luminosity, sometimes by more than an order of magnitude.

3.2. Galaxy Mergers

Our simulation suite includes 10 $z \sim 0$ mergers (see L14 for details) and 32 $z \sim 2$–3 mergers (see H13 for details). Figure 3 shows the time evolution of the observed and intrinsic UV slopes, IRX, log SFR, and the separation of the central supermassive BHs (a proxy for merger stage) for the M3M3e; the evolution of the other $z \sim 0$ merger simulations in which a strong starburst is induced is similar. There is a strong increase in the SFR at ∼2.3 Gyr, when the two galaxies are separated by less than 10 kpc. The peak of the starburst occurs at ∼2.5 Gyr. This phase is followed by a quiescent, "red and dead" phase owing to gas consumption during the starburst and AGN feedback. The time evolution of IRX is similar to that of the SFR. Interestingly, after ∼2.7 Gyr, IRX starts to increase because the intermediate-age and old stellar populations that dominate the dust heating in this phase (Hayward et al. 2014) emit increasingly less 1600 Å photons. Both the observed and intrinsic β values are relatively constant (∼−2) until the

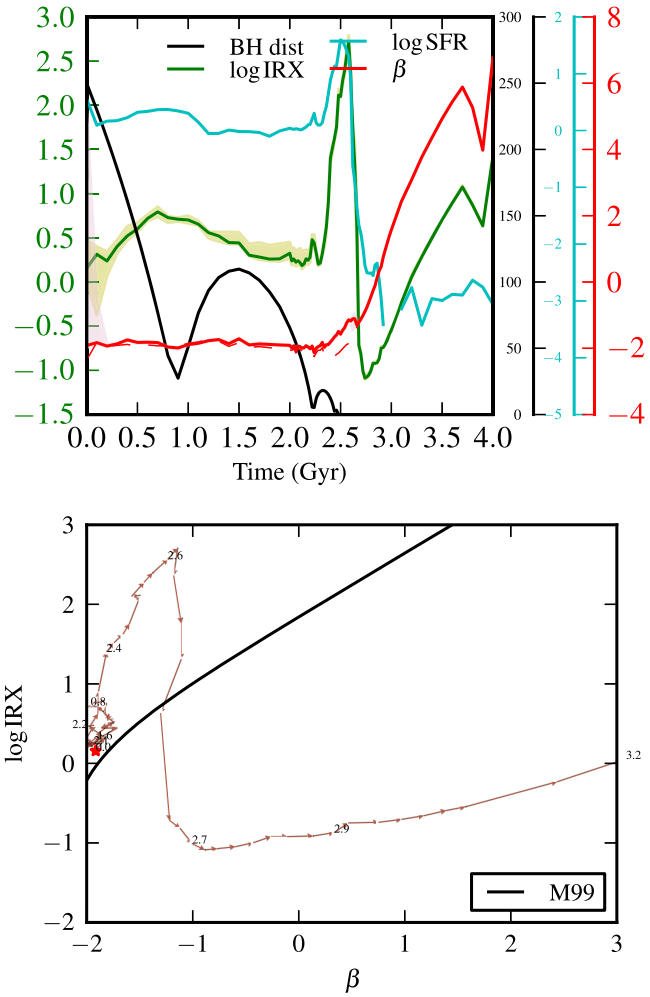

Figure 3. Same time evolution (top) and IRX–β (bottom) plots shown in Figure 1 but for a simulated $z \sim 0$ equal-mass merger system, M3M3e from L14. Top: the black line in this panel corresponds to the separation of the central supermassive BHs in kpc; this is a proxy for merger stage. There is a strong starburst induced near final coalescence (at ∼2.5 Gyr), immediately after which star formation is quenched because of gas consumption and AGN feedback. The time evolution of IRX is similar to that of the SFR. β has a relatively constant value of ∼−2 until the starburst, when it increases. Post-coalescence, $\beta > 0$ (i.e., the UV color is very red) owing to the star formation being quenched. The observed and intrinsic β values are almost identical except for during the starburst, and the variation in IRX and β with viewing angle is small; both of these results indicate that dust attenuation has minor effects on the UV slope in this case despite the system being a ULIRG at coalescence. Bottom: the merger is initially near the M99 relation, but it moves significantly above it during the coalescence-phase starburst. Subsequently, it moves rapidly below the relation as star formation is quenched and then moves to the right as its stellar population ages.

coalescence-phase starburst. During the starburst, the observed (intrinsic) β increases (decreases), and both increase in the post-starburst phase because star formation has been quenched and the stellar populations are passively evolving. The two β values are similar except during the starburst phase, and even then, the difference is modest compared with the $z \sim 2$–3 simulations. This indicates that dust reddening does not significantly affect the UV slope in this system despite the system having IRX > 1 (i.e., $L_{\rm FIR} > L_{\rm UV}$) for much of its evolution and being a ULIRG for a brief time during the starburst. For the same reason, the dispersion in IRX and β due to viewing angle is small.

The time evolution of the galaxy in the IRX–β plane is shown in the bottom panel of Figure 3. As in the previous

IRX–β plots, the points corresponding to different snapshots are connected by arrows to show the direction of time. The initial time snapshot is indicated with a red star, and the end of the simulation is marked with a red square. The system remains close to the M99 relation up until the start of the coalescence-phase starburst, during which there is a sharp increase in IRX without a significant change in the UV continuum slope. Consequently, the system moves above the relation. When star formation is quenched, the system moves rapidly below the relation, and it then moves to the right as its stellar populations ages.[12]

The time evolution of one of the $z \sim 2$–3 equal-mass mergers (b6b6m from H13) is shown in Figure 4. The top panel shows that the starburst induced at merger coalescence occurs at $t \sim 0.8$ Gyr. In contrast with the $z \sim 0$ merger examined above, star formation is not fully quenched: at the end of the simulation, the SFR is still $>10\ M_{\odot}\ \mathrm{yr}^{-1}$. The IRX value tends to track the SFR. For example, during the coalescence-induced starburst, IRX increases sharply, as in the $z \sim 0$ merger shown in Figure 3. Pre-coalescence, the UV continuum slope, β, increases from ~ -1.8 to ~ 0.3, and it then decreases by ~ 1 during the coalescence phase. It subsequently increases from ~ -0.7 to ~ 1.8, indicating that the galaxy transitions from blue to red, and then it decreases to ~ -0.3 over the remainder of the simulation. Owing to the lack of quenching, the galaxy remains blue. The difference between the observed (thick red line) and intrinsic (red dashed line) UV slopes is large throughout the simulation, reaching as high as ~ 3. This indicates that dust strongly affects the UV slope of this system. The viewing-angle-dependent dispersion in IRX and β (yellow and pink shaded regions, respectively) is very large in the post-starburst phase.

The bottom panel of Figure 4 shows the evolution of the $z \sim 2$–3 merger in the IRX–β plane. Initially, the system lies above the M99 relation. During the local minimum in the SFR at $t \sim 0.6$ Gyr, it moves onto the relation, and it subsequently moves back above the relation during the starburst induced at final coalescence of the system. Shortly after coalescence, it crosses the relation, and a few hundred megayears later, it returns to near the relation, where it remains until the end of the simulation because the galaxy is still actively forming stars at a rate $>10\ M_{\odot}\ \mathrm{yr}^{-1}$.

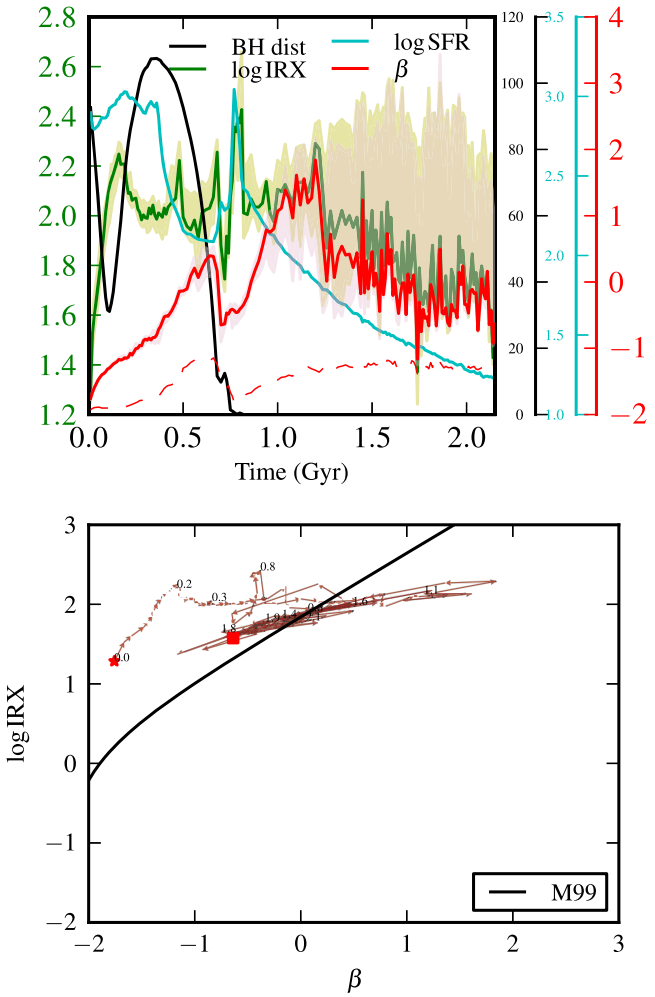

Figure 4. Similar to Figure 3, but for one of the simulated $z \sim 2$–3 equal-mass mergers from H13, b6b6m. Top: there is a strong starburst at merger coalescence ($\sim$800 Myr), after which the SFR decreases, but not as rapidly as in the $z \sim 0$ merger presented above. At the end of the simulation, SFR $\sim 20\ M_{\odot}\ \mathrm{yr}^{-1}$. As for the $z \sim 0$ merger, the evolution of IRX is similar to that of the SFR. However, the evolutions of both the observed and intrinsic β values differ qualitatively from the $z \sim 0$ case: the intrinsic β (red dashed line) increases as the relatively young stars present in the initial conditions age, decreases during the starburst, and then increases again. The time evolution of the observed β (thick red line) is similar except after $\sim$1.2 Gyr, when it decreases because dust reddening is becoming less significant. The difference between the observed and intrinsic UV slopes is large throughout the simulation, reaching as high as $\sim$3. This indicates that dust strongly affects the UV slope of this system. The viewing-angle-dependent dispersion in IRX and β (yellow and pink shaded regions, respectively) is very large in the post-starburst phase. Bottom: the system starts above the M99 relation and moves closer to it until the coalescence-phase starburst, when it moves back above the relation. The system then crosses the relation and moves back onto it, where it remains.

4. Impact of Dust Composition

In the above analysis, the MW-type dust model of Draine & Li (2007) was used in the radiative transfer calculations. It is worthwhile to investigate how the dust composition affects the predicted UV slope and IRX value. In particular, the SMC extinction curve of Draine & Li (2007) differs considerably from the MW curve in the UV: whereas the MW extinction curve exhibits a "bump" at $\sim$2175 Å, the SMC curve does not. Thus, the two dust models can lead to different dust reddening in the UV and consequently different observed UV slopes for a fixed intrinsic UV slope (i.e., fixed stellar population). The potentially drastic impact of dust grain composition on the positions of galaxies in the IRX–β plane has been discussed in the literature (e.g., Bell et al. 2002; Shapley 2011; Mao et al. 2014), but to the best of our knowledge, it has not been explored using the combination of hydrodynamical simulations and dust radiative transfer calculations that we employ in this work.

To investigate the impact of the dust grain composition, we performed radiative transfer on the $z \sim 0$ major merger simulation discussed above, M3M3e from L14, assuming SMC-type dust instead of the fiducial MW-type dust. The results of these radiative transfer calculations are compared with those of the standard MW-dust run in Figure 5. The top panel shows how the assumed dust grain model impacts the evolution of the merger in the IRX–β plane. The blue arrows follow the evolution of the system when SMC-type dust is

[12] Note that because of our use of common axes for all IRX–β plots, the system moves off the plot at 3.2 Gyr.

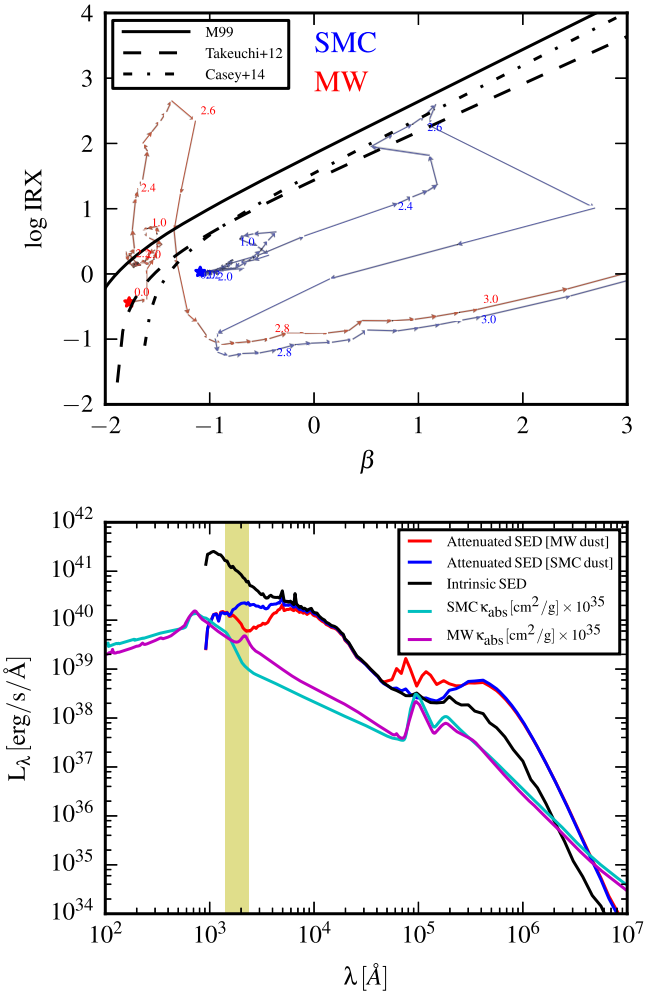

Figure 5. Demonstration of the impact of the assumed dust grain model on the final IRX and β values. Top: evolution of the M3M3e $z \sim 0$ major merger simulation in the IRX–β plane when MW-type (red arrows) and SMC-type (blue arrows) dust is used in the radiative transfer calculations. For the first ~2.7 Gyr of the simulation, when the system is actively forming stars, the assumed dust model *qualitatively* changes the evolution of the merger in the IRX–β plane. β is greater (i.e., the SED is redder) when SMC-type dust is assumed; IRX is relatively insensitive to the assumed dust model except for low IRX values. Bottom: comparison of the rest-frame SEDs of the M3M3e simulation at $t = 2.4$ Gyr. The intrinsic SED of the galaxy is shown in black. The attenuated SEDs (including dust reemission) predicted when MW-type and SMC-type dust are assumed are shown in red and blue, respectively. The yellow region indicates the wavelength range that is used to compute the UV slope. The absorption cross sections per unit mass of the MW (magenta line) and SMC (cyan line) dust models (renormalized as indicated in the legend) are also shown. It is clear that the two SEDs have very different UV slopes: β is negative (positive) when MW (SMC) dust is assumed. The extinction curves clearly show that the difference between the UV slopes obtained with the two dust models is due to the presence of the UV bump at 2175 Å in the MW curve and the change in the slope of the SMC curve in this wavelength range.

assumed, whereas the red arrows follow the evolution of the same system modeled with MW-type dust (this track is identical to that shown in the bottom panel of Figure 3). For the first ~2.7 Gyr of the simulation, when the system is actively forming stars (see Figure 3), the assumed dust model has a very significant impact on the position of the system in the IRX–β plane. In general, β is greater (i.e., the SED is redder) when SMC-type dust is assumed. For this reason, at fixed time, the merger can lie above the M99 relation if MW-type dust is assumed in the radiative transfer calculation but below it if SMC-type dust is used. The effect is greatest during the coalescence-phase starburst ($t \sim 2.4$–2.6 Gyr): when MW dust is assumed, the merger-driven starburst causes the system to move above the relation, but when SMC dust is assumed, the system moves closer to the relation during the starburst.

The bottom panel of Figure 5 illustrates why the assumed dust model has such a drastic impact on the system's position in the IRX–β plane. The black line is the intrinsic SED of the system at $t = 2.4$ Gyr, and the red (blue) line is the attenuated SED obtained when MW-type (SMC-type) dust is used in the radiative transfer calculation. The yellow shaded region denotes the wavelength range that is used to compute the UV slope (1300 Å $< \lambda <$ 2300 Å). The magenta and cyan curves show the absorption cross section per unit mass (in arbitrary units) for the MW- and SMC-type dust models, respectively. As is evident from comparing the SEDs, the 2175 Å feature present in the MW curve results in a more negative UV slope compared with the SMC dust model. The SMC curve starts to decrease more steeply with increasing wavelength near where the 2175 Å feature becomes evident in the MW curve, which exacerbates the difference in the UV slopes of the two SEDs. The difference between the two observed UV slopes, which is completely due to the assumed dust composition, is approximately 2. Although there is a large difference in the UV slope due to the dust grain model, the effect on IRX is modest for the following reasons: when IRX is high, the vast majority of UV photons from the young stars that dominate the intrinsic UV luminosity are absorbed regardless of whether MW- or SMC-type dust is assumed. Thus, $L_{\rm FIR}$ is insensitive to the dust model. Because the observed UV is dominated by unobscured stars (i.e., the UV and IR emission are essentially decoupled), $L_{\rm UV}$ is also not significantly affected. Thus, when IRX is high, it is not affected by the dust model. For example, comparing the $t = 2.4$ Gyr points in the IRX–β plane in the top panel reveals that the two SEDs have the same IRX value but very different UV slopes. Thus, the difference in β is the primary driver of the difference in the IRX–β evolution.

After the starburst, when star formation has been quenched, the choice of dust model matters little. The MW track tends to be slightly above the SMC track because for fixed dust column density, the MW dust model yields a greater optical depth in the UV–optical regime. When IRX is low (as it is in this phase), and thus the galaxy is not opaque to UV photons, the increase in the optical depth caused by assuming MW-type rather than SMC-type dust can lead to a non-negligible increase in the IR luminosity and decrease in the observed luminosity, thus causing a non-negligible (but small) increase in IRX.

Note that as shown in the bottom panel of Figure 5, the MW and SMC dust extinction curves are almost identical over the wavelength range of ~500–1500 Å. Consequently, for a given dust column density, the UV slope in this wavelength range should be reddened by the same amount regardless of whether the dust is MW-like or SMC-like. For this reason, it may be possible to fit the UV slope between the Lyman limit and 1500 Å rather than in the canonical range (1300 Å $< \lambda <$ 2300 Å) to mitigate the uncertainty associated with dust composition.

5. Dispersion in the UV Slope

Various factors can in principle lead to dispersion in the IRX–β plane, including dust geometry (Cortese et al. 2006), SFH (Kong et al. 2004), the mean age of the stellar population (Mao et al. 2012; Grasha et al. 2013), or stellar

mass (Álvarez-Márquez et al. 2016). Boquien et al. (2012) studied a set of face-on normal star-forming spiral galaxies to understand why normal star-forming galaxies deviate from starburst galaxies in terms of their positions in the IRX–β plane. They found that the intrinsic dispersion in the UV slope correlates most strongly with the distance from the M99 relation. Kong et al. (2004) suggest that the dispersion results from differences in the SFHs of galaxies (by considering the birth rate parameter b, which is the ratio of the current to past SFR; note that this parameter can be quite sensitive to how one defines "current" when the SFR is highly variable; e.g., Sparre et al. 2015a). Both studies point to the importance of underlying SFH for the observed dispersion of galaxies in the IRX–β plane. Álvarez-Márquez et al. (2016) studied a stacked sample of LBGs at $z \sim 3$ and concluded that stellar mass best predicts deviations from the IRX–β relation. They found that more massive LBGs have bluer colors and higher dust attenuation. This is in agreement with the trend observed by Casey et al. (2014) for DSFGs. Mao et al. (2012) studied spatially resolved normal star-forming galaxies from the SINGS (Kennicutt et al. 2003; Dale et al. 2007) sample by separating a galaxy into UV-emitting clusters and background disk and bulge regions. The found that the mean stellar population age contributes significantly to the dispersion in the IRX–β plane, and the location of the galaxy as a whole in the IRX–β plane is determined largely by the local background regions.

We can distinguish between scatter due to different SFHs and that due to dust geometry by comparing the dispersions in the intrinsic and observed (i.e., attenuated) β values because the intrinsic UV slope depends only on the SFH, whereas the latter also includes the viewing-angle-dependent effects of dust. In Figure 6, we show 2D histograms of the intrinsic (top panel) and observed (bottom panel) β values versus specific SFR (sSFR $\equiv$ SFR$/M_\star$). All simulations analyzed in this work (i.e., both isolated disks and mergers at both $z \sim 0$ and $z \sim$ 2–3) are shown here. Both the intrinsic and observed β values are anticorrelated with sSFR. This implies that in the most actively star-forming systems, young, massive stars dominate the UV emission and thus make the UV slope blue. Moreover, the dispersion at fixed sSFR is anticorrelated with sSFR, which implies that the past SFH affects β less in actively star-forming systems. A comparison of the two panels reveals that for galaxies with sSFR $\gtrsim 10^{-12}$ yr^{-1}, dust attenuation causes β to increase (i.e., the UV slope to become redder), whereas for systems with lower sSFR values, the intrinsic and observed β distributions are similar. The bifurcation evident for sSFR $\lesssim 10^{-11}$ yr^{-1} is due to the inclusion of both low- and high-redshift simulations: at fixed sSFR, the $z \sim 0$ simulations tend to have lower β values.

Figure 7 shows the dispersion in β, σ_β, versus sSFR. σ_β is computed by binning the SEDs in terms of their corresponding sSFR values and then dividing the difference between the 16th and 84th percentiles by two; for a normal distribution, this measure would equal the standard deviation. σ_β thus incorporates variations due to viewing angle, the time evolution of a given system, and the differences among the simulations. The solid (dashed) lines correspond to the observed (intrinsic) β values, and red (blue) denotes $z \sim 0$ ($z \sim$ 2–3). This figure reinforces our conclusion from Figure 6 that the dispersions in both the intrinsic and observed β values are anticorrelated with sSFR. Considering the $z \sim 0$ simulations, we note that the

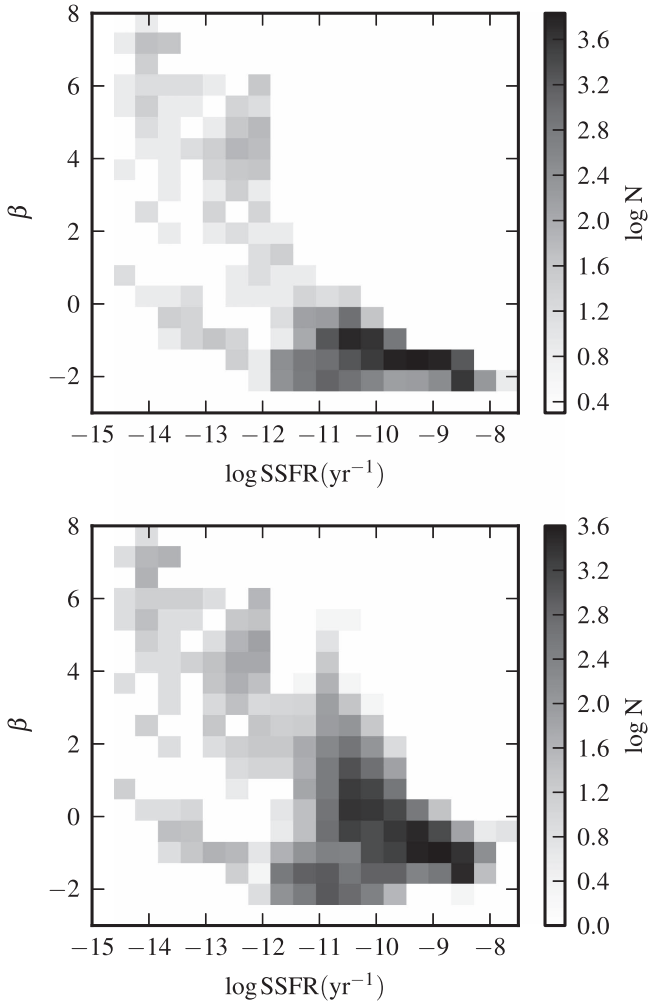

Figure 6. 2D histograms of the intrinsic (top) and observed (i.e., attenuated; bottom) β values vs. log (sSFR/yr^{-1}) for all simulated galaxies analyzed in this work (i.e., both the $z \sim 0$ and $z \sim$ 2–3 data sets). Note that the color bar indicates the logarithm of the number of SEDs in a given pixel. Both the intrinsic and observed β values are anticorrelated with sSFR because in more actively star-forming galaxies, young, massive stars dominate the luminosity and cause the UV slope to be blue. The scatter at fixed sSFR is also anticorrelated with sSFR because the past SFH does not affect the UV slope if very young stars dominate the UV luminosity. A comparison of the two histograms reveals that for galaxies with high sSFR, dust attenuation causes the observed UV slope to be redder than the intrinsic slope. For passive systems, β is essentially unaffected by dust attenuation. The bifurcation evident for sSFR $\lesssim 10^{-11}$ yr^{-1} is due to the inclusion of both low- and high-redshift simulations: at fixed sSFR, the $z \sim 0$ simulations tend to have lower β values.

dispersions in the intrinsic and observed β values differ by a modest amount, and the difference is greater at high sSFR. Computing the difference between the intrinsic and observed σ_β values in quadrature, which characterizes the contribution of dust attenuation to the dispersion (related to both viewing-angle-related effects and differences in dust geometry among different time snapshots and simulations), we find that dust adds at most 0.4 to σ_β, and it typically adds $\lesssim$0.2. Thus, in the actively star-forming $z \sim 0$ simulations, dust attenuation and SFH variations contribute comparably to the dispersion in the observed β values, whereas in systems with lower sSFR, SFH variations dominate the dispersion.

In contrast, for the $z \sim$ 2–3 simulations, the difference between the intrinsic and observed β dispersions is significant. Again computing the difference in the σ_β values in quadrature,

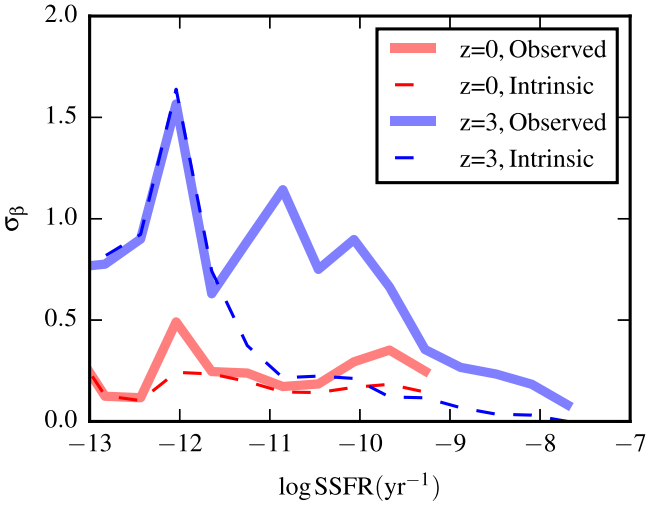

Figure 7. Dispersion in β vs. log (sSFR/yr^{-1}). σ_β is defined by dividing the difference between the 16th and 84th percentile values of the β distribution (including all simulations and viewing angles) in a given sSFR bin by 2. The red (blue) lines correspond to the $z \sim 0$ ($z \sim$ 2–3) simulations. The solid (dashed) lines denote the dispersion in the observed (intrinsic) β values. The dispersion in both the intrinsic and observed β values is anticorrelated with sSFR, as already observed from Figure 6. In the $z \sim 0$ simulations with high sSFR, SFH variations and dust attenuation contribute comparably to the dispersion; in lower-sSFR systems, SFH history variations dominate. In contrast, in the $z \sim$ 2–3 simulations with sSFR $\gtrsim 10^{-11.5}$ yr^{-1}, the β variation due to dust attenuation (related to both viewing-angle-related effects and differences in dust geometry among different time snapshots and simulations) is much greater than that due to SFH variations. For actively star-forming galaxies, the dispersion in the observed β is greater for the $z \sim$ 2–3 simulations than for the $z \sim 0$ simulations. Our results suggest that even if low-redshift galaxies obey a relatively tight IRX–β relation, this should not be the case at higher redshifts.

we find that the variation due to dust attenuation dominates that due to SFH variations in all bins with sSFR $\gtrsim 10^{-11.5}$ yr^{-1}, in contrast with the $z \sim 0$ simulations. For systems with lower sSFR values, the intrinsic and observed β dispersions are almost identical, which indicates that SFH variations dominate the dispersion. Finally, we note that for actively star-forming galaxies, the dispersion in the observed β values at fixed sSFR is greater for the $z \sim$ 2–3 simulated galaxies than for those intended to be representative of $z \sim 0$ galaxies. Consequently, our results suggest that even if low-redshift galaxies obey a tight IRX–β relation (i.e., the M99 relation), this is unlikely to be the case at higher redshift. Moreover, the above results suggest that the sought-after "second parameter" (i.e., what property best predicts deviations from the M99 relation) may depend on the galaxy type and redshift considered.

6. Relationship between IRX and UV Optical Depth

One benefit of our simulations is that because the intrinsic spectrum is perfectly known, we can directly measure the effective optical depth at arbitrary wavelengths. For this work, it is of interest to consider how the optical depth in the UV is related to IRX. We specifically consider the optical depth at 1500 Å, $\tau_{1500\,\text{Å}} \equiv -\ln(L_{1500,\text{observed}}/L_{1500,\text{intrinsic}})$. Figure 8 shows the distribution of the simulated galaxies in the log IRX–$\tau_{1500\,\text{Å}}$ plane. The bins are color-coded according to the logarithm of the number of galaxies in the bin, as indicated by the color bar. For $\tau_{1500\,\text{Å}} \gtrsim 2$ (i.e., when escape fraction at 1500 Å is $\lesssim$10%), log IRX and $\tau_{1500\,\text{Å}}$ are tightly correlated. However, for fixed $\tau_{1500\,\text{Å}} \lesssim 2$, IRX can vary by multiple orders

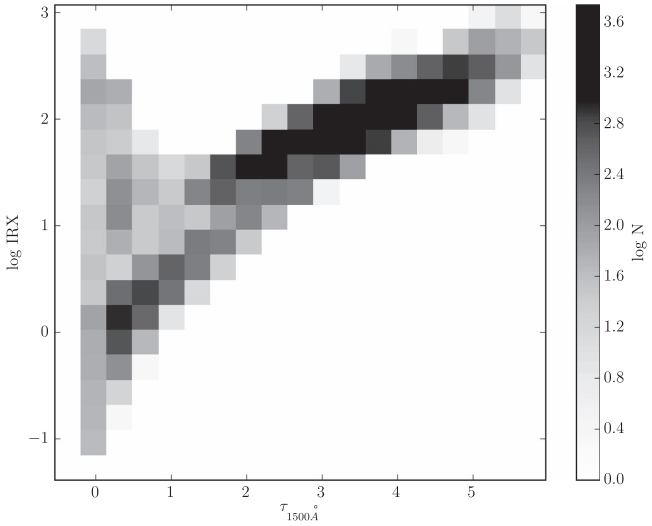

Figure 8. 2D histogram of the logarithm of IRX vs. effective optical depth at 1500 Å, $\tau_{1500\,\text{Å}}$. The color bar indicates the number of simulation snapshots in each bin. For $\tau_{1500\,\text{Å}} \gtrsim 1$, the correlation between the two quantities is relatively tight. However, for fixed $\tau_{1500\,\text{Å}} \lesssim 1$, the regime in which the UV continuum escape fraction is non-negligible, IRX can vary by multiple orders of magnitude. This large scatter implies that the UV continuum escape fraction cannot be reliably inferred from the value of IRX.

of magnitude. Consequently, our simulations indicate that IRX cannot be used to reliably infer the UV optical depth in the regime of most interest (when the UV escape fraction is high).

7. DSFGs in the IRX–β Plane

Many DSFGs at $z \sim$ 2–3 have very blue UV continuum slopes (i.e., negative β values) and high IRX values (Casey et al. 2014), which makes them lie above the M99 relation. Very blue and dusty systems were also found in a study of 16 individually *Herschel* PACS 100 and 160 μm detected LBGs at $z \sim 3$ (Oteo et al. 2013). Although these samples are biased by the IR selection, the results may indicate that massive galaxies tend to have bluer UV slopes and higher IRX values compared with less massive galaxies (Álvarez-Márquez et al. 2016). Moreover, where DSFGs reside in the IRX–β plane may yield insights into the origin of their extremely high SFRs: Casey et al. (2014) argue that the fact that DSFGs lie above the M99 relation is evidence that they are short-timescale starbursts rather than "main-sequence" galaxies (i.e., galaxies near the approximately linear SFR–stellar mass relation).

We can directly address this question using our simulation suite. In Figure 9, we show the locations of our simulated $z \sim$ 2–3 DSFGs in the IRX–β plane; the top panel shows the results of the simulated $z \sim$ 2–3 mergers, whereas the bottom panel shows the simulated $z \sim$ 2–3 isolated disk galaxies. The orange, green, and blue points correspond to simulated LIRGs ($10^{11} < L_{\text{IR}}/L_\odot < 10^{12}$), ULIRGs ($10^{12} < L_{\text{IR}}/L_\odot < 10^{13}$), and hyper-LIRGs (HyLIRGs; $L_{\text{IR}} > 10^{13}\,L_\odot$), respectively. (There are no blue points in the bottom panel because the simulated isolated disks never attain $L_{\text{IR}} > 10^{13}\,L_\odot$.) In both panels, the red points correspond to real $z \sim$ 2.5–3.5 DSFGs selected from the COSMOS survey (Scoville et al. 2007), the IRX and β values of which were presented in Casey et al. (2014).

In both panels, the regions in the IRX–β plane spanned by the real and simulated DSFGs are broadly consistent, although

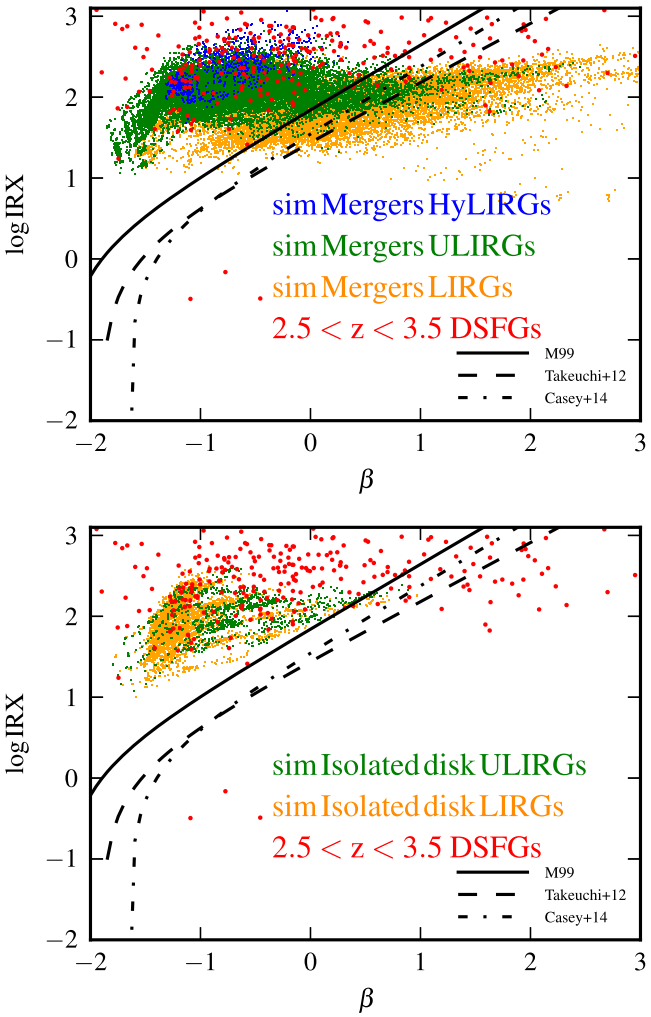

Figure 9. Positions of our simulated $z \sim 2$–3 DSFGs in the IRX–β plane. The mergers (isolated disks) are shown in the top (bottom) panel. The points are color-coded according to IR luminosity: orange, green, and blue points correspond to simulated LIRGs ($10^{11} < L_{\rm IR}/L_{\odot} < 10^{12}$), ULIRGs ($10^{12} < L_{\rm IR}/L_{\odot} < 10^{13}$), and hyper-LIRGs (HyLIRGs; $L_{\rm IR} > 10^{13}\,L_{\odot}$), respectively. In both panels, the red points correspond to the observed $z \sim 2.5$–3.5 DSFGs from Casey et al. (2014). It is evident that both the simulated mergers and isolated disk can become (U)LIRGs during their evolution. However, only the mergers can reach $L_{\rm IR} > 10^{13}\,L_{\odot}$ and log IRX > 2.5. Because the simulated isolated disks overlap with observed DSFGs in the IRX–β plane, the fact that some real DSFGs lie well above the M99 relation is not evidence that they are powered by short-lived starbursts.

for log IRX $\gtrsim 2.5$, the specific simulations used here do not span the full range of β spanned by real DSFGs, which can be both slightly bluer and significantly redder than the simulated galaxies (see also Wuyts et al. 2009). For the mergers (top panel), the offset from the M99 relation tends to increase with IR luminosity; all of the simulated HyLIRGs are well above the M99 relation, which indicates that despite having effectively all of their luminosity absorbed and reradiated by dust ($L_{\rm IR}/L_{\rm UV} \gtrsim 100$), they have blue UV continuum slopes. The reason for our simulated DSFGs having blue UV colors is that in these IR-luminosity-selected systems, the UV and IR are essentially decoupled: the IR luminosity is powered by stars that are invisible in the UV, whereas the UV emission originates from a "frosting" of unobscured young stars. This holds for both the simulated mergers and isolated disks.

Notably, the bottom panel shows that our simulated gas-rich $z \sim 2$–3 isolated disk galaxies are similar to DSFGs in terms of their location in the IRX–β plane. These galaxies are not undergoing merger-driven starbursts by construction. Thus, our results demonstrate that the position of DSFGs in the IRX–β plane does not necessarily imply that they are short-lived starbursts, contrary to the claim of Casey et al. (2014); instead, DSFGs well above the M99 relation can be steadily star-forming, massive, gas-rich disks as long as they are sufficiently dust obscured, which is a natural outcome for high-gas-fraction, metal-enriched galaxies. Consequently, high-z DSFGs may represent a heterogeneous population of massive, gas-rich, steadily star-forming galaxies, merger-induced starbursts, and obscured AGNs (e.g., Hopkins et al. 2010; Hayward et al. 2011, 2012, 2013a, 2013b; da Cunha et al. 2015; Koprowski et al. 2016). We do find that all of the simulated galaxies with $L_{\rm IR} > 10^{13}\,L_{\odot}$ (see also Hopkins et al. 2010) and, of the lower-luminosity simulated galaxies, those with the highest IRX values (log IRX $\gtrsim 2.5$) are exclusively mergers, and in the simulations, these HyLIRGs are typically powered by combination of merger-induced starbursts and obscured AGNs (Roebuck et al. 2016). However, we cannot determine whether these are physical limits or simply artifacts of the specific parameter space spanned by the simulations.

However, it should be noted that the IRX and β values plotted in Figure 9 are those obtained when MW-type dust is used in the radiative transfer calculations. As we have shown in Section 4, using MW-type dust yields more negative UV slopes than when SMC-type dust is assumed. Consequently, if we were to assume SMC-type dust when performing the radiative transfer calculations, our simulated galaxies might not populate the low-β, high-IRX region that is occupied by a significant fraction of real DSFGs. Thus, it is possible that the location of DSFGs in the IRX–β plane may encode information regarding their dust composition. This is an interesting topic that could be explored with future simulations.

8. Comparison with Previous Work

We now compare our results with those of some previous theoretical works. The evolutionary tracks of galaxies in the IRX–β plane were previously studied in the context of semianalytic models coupled with radiative transfer calculations assuming simplified geometries (GRASIL; Silva et al. 1998) by Granato et al. (2000, hereafter G00). G00 find that in the early stages of a starburst, the UV slopes of their model galaxies become bluer (more negative). When the SFR decreases, and consequently older stellar populations dominate the intrinsic UV slope, the system evolves toward more positive (redder) β and lower IRX values. In G00's model, the strength of the burst defines the evolutionary path on the IRX–β plane. Stronger starbursts have only slightly negative or positive (red) UV slopes ($\beta \gtrsim -0.5$), initially because they experience high attenuation on timescales longer than the exponential decay timescale of the SFR and later because the stellar population has turned old. Their IRX values are generally $\gtrsim$10. In contrast, weaker starbursts span a larger dynamical range in the IRX–β plane because these galaxies quickly exhaust their gas, which causes the attenuation to decrease rapidly and makes them evolve toward low IRX and negative β values. We note that G00 assume MW dust, as have we in our fiducial calculations, and can reproduce the Calzetti

attenuation law, despite the conclusion of Gordon et al. (1997) that SMC-type dust is needed to reproduce the Calzetti law.

Unlike G00, when a strong burst occurs in our simulations (e.g., the M3M3e simulation shown in Figure 3), the system moves almost vertically in the IRX–β plane because IRX increases by a large amount, whereas the UV slope becomes only slightly redder. The two results might seem contradictory, but the difference lies in how we define the onset of starburst. If we consider the evolution of the M3M3e merger system starting with the peak of the starburst (during the coalescence phase), which corresponds to G00's definition (because they assume an exponentially declining SFH for the burst), we see a similar trend: the galaxy maintains a relatively flat UV slope while moving toward lower IRX values. The further evolution of the system when the stellar population becomes old is similar to the starbursts modeled in G00. The starbursts modeled by G00 lie on the M99 relation as long as the age of the starburst is $\lesssim$50 Myr. However, a comparison of Figure 7 of G00 with Figure 9 indicates that the starbursts in the G00 model never occupy the high-IRX, low-β region spanned by both our simulated DSFGs and observed DSFGs. This discrepancy may be a result of the parameter space that they considered, their assumption of an exponentially declining SFH for bursts, and/or the simplified geometry assumed in their radiative transfer calculations.

Khakhaleva-Li & Gnedin (2016) performed radiative transfer on galaxies formed in cosmological simulations from the "Cosmic Reionization on Computers" (CROC) project (Gnedin 2014) to compare the UV and IR properties of their simulated $z > 5$ galaxies, including their positions in the IRX–β plane, with observations. They find that in order to match the observed UV luminosity function at $z > 5$, they must include the effects of dust destruction via sublimation in supernova shocks; otherwise, their galaxies are too dusty and thus UV-faint to explain the observed UV luminosity function. Their simulated galaxies lie near the M99 relation, although IRX can vary by approximately an order of magnitude at fixed β. The locus of their simulated galaxies in the IRX–β plane is consistent with some $z > 5$ galaxies for which both β and IRX have been measured (Capak et al. 2015), but the galaxies with log IRX $\gtrsim$ 0.5 from Capak et al. (2015) and the $z \sim 7.5$ galaxy presented by Watson et al. (2015) lie outside the region spanned by the simulated galaxies. Because our simulations and theirs cover disjoint regions of parameter space in terms of redshift and mass, it is not possible to make detailed comparisons between our results and theirs. However, their results highlight the potential importance of dust destruction for accurately predicting the UV properties of simulated galaxies and provide motivation for future studies that include more complex treatments of dust production, growth, and destruction.

9. Implications for Observations

Our simulation results suggest that there is not a tight relation between IRX and β that applies to all galaxies at all redshifts. The $z \sim 0$ simulated galaxies tend to lie near the M99 relation, which was determined based on observations of galaxies in the local universe. However, during merger-induced starbursts, even the $z \sim 0$ galaxies can depart significantly from the relation: because IRX increases significantly but β is almost unaffected, the $z \sim 0$ merger-induced starbursts, such as that shown in Figure 3, tend to lie above the M99 relation. The $z \sim 2$–3 simulations—of both disk galaxies and mergers—deviate more significantly from the M99 relation: even when they are not undergoing starbursts, they tend to lie above the relation.

These results are consistent with observational works that have demonstrated that some classes of galaxies deviate significantly from the M99 relation. As already discussed above, observed DSFGs tend to lie above the M99 relation and do not exhibit any relationship between IRX and β (e.g., Bell et al. 2002; Goldader et al. 2002; Howell et al. 2010; Casey et al. 2014). Conversely, some galaxies lie significantly below the M99 relation (i.e., have lower IRX than expected from the relation given their β). This was demonstrated for the lensed galaxies cB58 at $z \sim 2.7$ (Pettini et al. 2000) and the Cosmic Eye (Smail et al. 2007) at $z \sim 3.07$. Similarly, Reddy et al. (2012) found that young systems (age $<$100 Myr) at $z \sim 2$ lie below the M99 relation.

Moreover, we have demonstrated that the dust composition —specifically the strength of the 2175 Å feature—can have a very dramatic effect on the UV slope. Consequently, extrapolation of the locally calibrated IRX–β relation to regimes for which it is not observationally constrained may be problematic if, e.g., the dust composition of high-redshift galaxies is significantly different from that of $z \sim 0$ galaxies. How the strength of the UV bump varies with galaxy properties and redshift is still poorly understood, but there are some useful observational constraints. The commonly employed Calzetti et al. (1994) attenuation law, which was defined based on observations of local-universe starburst galaxies, does not exhibit a UV bump. Based on a study of ~10,000 $z < 0.1$ star-forming galaxies, Battisti et al. (2016) derived an average attenuation curve that does not have a significant 2175 Å feature. However, Motta et al. (2002) presented evidence for the UV bump in a gravitationally lensed normal early-type galaxy at $z = 0.83$. Since then, other detections for high-redshift galaxies have been reported in the literature (Noll et al. 2009; Buat et al. 2011; Kriek & Conroy 2013). Conroy et al. (2010) studied attenuation as a function of inclination using a sample of nearby disk galaxies. Trends due to dust attenuation alone can be identified in such studies because stellar population properties are unrelated to inclination. The trends observed by Conroy et al. (2010) suggest the presence of the 2175 Å feature with an amplitude ~80% of the canonical MW value. Studying ~30 galaxies at $z > 1$, Buat et al. (2011) detected a significant UV bump at 2175 Å but with an amplitude ~35% of that of the MW extinction curve. For a sample of galaxies in the redshift range $0.5 < z < 2$, Kriek & Conroy (2013) found evidence for a UV bump whose strength increases with the slope of the attenuation curve. Given the above mixed and perhaps even contradictory results, more effort clearly needs to be invested in understanding how the composition of dust varies across cosmic time and among different galaxy populations.

Because the intrinsic spectrum is well described by a single power law over the rest-frame wavelength range ~1100–3600 Å, in the absence of dust attenuation, one can in principle recover the intrinsic β equally well using any rest-frame wavelengths within the aforementioned range (but choosing more widely separated wavelengths is of course beneficial for providing a larger "lever arm"). It may be possible to minimize or eliminate the effect of the 2175 Å feature identified in Section 4 by carefully selecting the bands employed to calculate β according to a galaxy's redshift. Specifically, for some redshifts, one could "straddle" the feature

using, e.g., the NUV–u color: at $z = 0.4$, this would be equivalent to fitting a power law to the fluxes at 1570 and 2600 Å, thus minimizing the influence of the 2175 Å feature. At $z = 1$, these bands correspond to rest-frame wavelengths of 1100 and 1820 Å. For higher redshifts, other filter combinations could be used. Although the difference in the slope of the attenuation curve between the MW and SMC models would not be addressed by such an approach, much of the uncertainty owing to the dust composition, which is especially poorly constrained for high-redshift galaxies, would be ameliorated.

The IRX–β relation is often applied to classes of galaxies (in terms of properties such as mass and redshift) for which the IRX–β relation is not directly constrained. The above discussion suggests that it is unlikely that there is a universal IRX–β relation; instead, variations in both global galaxy properties and dust composition can cause significant deviations from the M99 relation. Constraints on the SFH of the universe at $z \gtrsim 3$ are almost exclusively based on dust-correcting the UV luminosity using the M99 relation to obtain the SFR (e.g., Bouwens et al. 2009, 2012, 2014; Dunlop et al. 2012; Finkelstein et al. 2012). Use of the M99 relation can cause one to underestimate the SFRs of galaxies that lie above the M99 relation, such as DSFGs, possibly by multiple orders of magnitude. If such galaxies contribute non-negligibly to the SFH of the universe, the UV-based constraints would not recover the true SFR density. For this reason, it is crucial to obtain direct constraints on obscured star formation via rest-frame IR observations of galaxies at higher redshift ($z \gtrsim 3$) and with less extreme SFRs ($\lesssim$100 $M_{\odot}$ yr^{-1}) than has been possible with surveys performed with, e.g., the JCMT and *Herschel*. ALMA is an excellent tool with which to address this challenge, and some very interesting constraints have already been obtained (e.g., Capak et al. 2015; Watson et al. 2015), but more work needs to be done.

10. Limitations and Future Work

Although our simulations have yielded insights into the evolution of galaxies in the IRX–β plane, they are of course subject to some limitations. First, they are idealized noncosmological simulations. The advantage of such simulations is that they enable one to explore a significant region of the relevant parameter space while achieving the resolution necessary to perform radiative transfer on the simulated galaxies. However, their noncosmological nature implies that effects such as cosmological gas accretion and subsequent mergers are not included, and the demographics of our simulation suite are not cosmologically representative. Unfortunately, given the resolution limitations of state-of-the-art cosmological hydrodynamical simulations (see, e.g., the discussions in Sparre et al. 2015b; Sparre & Springel 2016), such simulations are currently not useful for modeling the propagation of UV light on galaxy scales and thus the IRX–β relation.

Moreover, we employ the Springel & Hernquist (2003) subresolution model for the structure of the ISM and the effects of supernova feedback. Although this model is still widely used, simulations that resolve the small-scale structure of the ISM and feature more sophisticated, explicit treatments of stellar feedback have been presented (e.g., Hopkins et al. 2014; Agertz & Kravtsov 2015). In such simulations, properties such as disk scale heights, which may be determined by stellar-feedback-driven turbulent pressure support (e.g., Faucher-Giguère et al. 2013; Hayward & Hopkins 2017) or cosmic rays (e.g., Booth et al. 2013), are likely more realistic than in the simulations used in this work. Altering the vertical structure of the gas—and thus dust—disks in the simulations could affect our predicted IRX–β relation.

Additionally, given that such simulations resolve the ISM on scales of approximately an order of magnitude smaller than our simulations, they may more faithfully capture how UV light propagates in real galaxies than the present simulations do. The present simulations may not correctly capture the relative amount of UV emission attenuated by dust local to star-forming regions instead of "diffuse" dust. The discrepancy between the 24 and 70 μm flux ratios of the simulated galaxies presented in Jonsson et al. (2010) and observed galaxies may be evidence for such a discrepancy (although the 24 μm emission, in particular, is sensitive to other uncertain aspects of the radiative transfer calculations, such as nonequilibrium emission from stochastically heated very small grains). It will be very interesting to investigate how the balance between local and diffuse attenuation differs in the aforementioned simulations that resolve the small-scale ISM and to compare their colors with those of real galaxies.

Higher-resolution simulations with explicit stellar feedback also self-consistently generate galactic winds (Muratov et al. 2015). The lack of winds in our simulations may cause, e.g., the time evolution of the gas and metal content of our galaxies to be somewhat unrealistic. However, this is less of a concern for the idealized noncosmological simulations used here than for cosmological simulations because the cosmological evolution of the baryon and metal content of galaxies—which is determined by a combination of inflows, outflows, and self-enrichment—is intentionally not modeled in our work. Instead, we constructed initial conditions by hand such that our simulated galaxies have properties such as gas fractions and metallicities that are roughly consistent with empirical constraints (see, e.g., Cox et al. 2008; Rocha et al. 2008, for details).

For the above reasons, it would be of great interest to repeat our analysis using such simulations, and this work is under way. However, because of the high computational expense of cosmological zoom-in simulations that resolve GMC scales and include explicit stellar feedback, it is a challenge to construct large samples of simulations for statistical studies. Moreover, the cosmological nature of the simulations and the chaotic behavior caused by explicit stellar feedback imply that controlled studies of the effect of a single parameter (e.g., gas fraction) are challenging. For these reasons, idealized simulation suites such as that used in this work are still useful for some studies.

Finally, we have not employed a detailed model for dust production and destruction, but rather assumed that the dust-to-metal density ratio is constant. As Khakhaleva-Li & Gnedin (2016) have noted, the details of dust production and destruction may have important implications for the UV and IR properties of simulated galaxies, especially in low-metallicity galaxies at high redshift. It would thus be useful to perform an analysis similar to ours using simulations that include a detailed treatment of the relevant dust production and destruction channels (e.g., McKinnon et al. 2016a, 2016b).

11. Conclusions

We have analyzed a set of 51 hydrodynamical simulations of idealized (i.e., noncosmological) galaxies, including both

isolated disk galaxies and mergers at both $z \sim 0$ and $z \sim 2$–3, on which dust radiative transfer was performed in post-processing to yield UV–millimeter SEDs, from which we measured the UV continuum slope (β) and IRX $\equiv L_{\rm IR}/L_{\rm UV}$. This method enables us to forward-model the evolution of the simulated galaxies in the IRX–β plane. Our primary conclusions are as follows:

1. The simulated $z \sim 0$ isolated disk galaxies tend to reside near the M99 relation, whereas the $z \sim 2$–3 disks are generally above it (i.e., at fixed β, they have higher IRX values than expected from the M99 relation).
2. In the simulated mergers, when a strong starburst is induced near coalescence, the systems tend to move almost vertically in the IRX–β plane because IRX increases significantly but β remains similar. In the post-starburst phase, if star formation is quenched via gas consumption and AGN feedback, IRX decreases rapidly, and β increases (i.e., the UV slope becomes redder) as the stellar population ages.
3. The dust type that is assumed in the radiative transfer calculations drastically impacts the resulting "observed" UV continuum slope. MW-type dust, for which the extinction curve exhibits a "bump" at 2175 Å, results in a significantly more negative (i.e., bluer) UV slope than SMC-type dust, for which the extinction curve does not exhibit the 2175 Å bump and has a steeper slope in the UV compared with MW-type dust. When the simulated galaxies are actively forming stars, the effects of the assumed dust model on the galaxies' positions in the IRX–β plane are more significant than the dispersion due to differences in galaxy properties, such as mass and SFH, the dispersion due to viewing angle, and model uncertainties other than the dust composition.
4. The dispersion in both the intrinsic and observed β values is anticorrelated with sSFR. Considering actively star-forming simulated galaxies, dust attenuation dominates the dispersion in β for the $z \sim 2$–3 simulations, whereas in the $z \sim 0$ simulations, the contributions from SFH variations and dust attenuation are similar. At low sSFR, SFH variations dominate the β dispersion at both redshifts. These results suggest that the sought-after "second parameter" (i.e., what property best predicts deviations from the M99 relation) should depend on the galaxy type and redshift considered.
5. When sSFR $\gtrsim 10^{-11.5}\,{\rm yr}^{-1}$, the dispersion in the observed β at fixed sSFR is higher in the $z \sim 2$–3 simulations than in the $z \sim 0$ simulations. This result indicates that even if a relatively tight IRX–β relation is obeyed by low-redshift galaxies, this should not be the case for galaxies at higher redshift.
6. IRX is well correlated with the effective optical depth at 1500 Å when the latter quantity is $\gtrsim$2. However, when the UV escape fraction is non-negligible (the regime of most interest for, e.g., studies of reionization), IRX can vary by multiple orders of magnitude at fixed optical depth.
7. The simulated $z \sim 2$–3 DSFGs tend to lie above the M99 relation (i.e., have high IRX values yet blue UV slopes), similar to observed $z \sim 2$–3 DSFGs (although this result may be sensitive to the assumed dust model). Consequently, in contrast with some previous claims in the literature, the position of DSFGs in the IRX–β plane is not evidence that they are powered by short-lived starburst events; rather, they may also be "main-sequence" galaxies as long as they are sufficiently dust obscured. However, the simulations with $L_{\rm IR} > 10^{13}$ and/or log IRX $\gtrsim 2.5$ are exclusively merger-driven starbursts, sometimes with a significant contribution from obscured AGNs.

Our work adds to the growing consensus that a well-defined IRX–β relation is not obeyed by all galaxy populations. DSFGs, in particular, can deviate significantly, and inferring the SFR by dust-correcting the UV luminosities of such galaxies using the M99 or a different IRX–β relation would cause their SFRs to be underestimated, potentially by multiple orders of magnitude. Consequently, the UV-inferred SFR density may be more unreliable than is generally believed. This highlights an urgent need for current and future observatories, such as ALMA, the Large Millimeter Telescope, and the Chajnantor Submillimeter Survey Telescope (Padin 2014), to directly constrain the obscured SFRs of galaxies at higher redshift and lower SFRs than are probed by existing surveys.

We thank Patrik Jonsson for insightful discussions. We are thankful to Caitlin Casey for providing us with data in electronic form. The Flatiron Institute is supported by the Simons Foundation. C.C.H. is grateful to the Gordon and Betty Moore Foundation for financial support. This work was partially supported by NASA's Astrophysics Data Analysis Program under grant NNX15AE54G. The computations in this paper were run on the Odyssey cluster supported by the FAS Division of Science, Research Computing Group at Harvard University. This research has made use of NASA's Astrophysics Data System Bibliographic Services and the arXiv.org preprint server.

Appendix A
Convergence with Respect to Hydrodynamical Resolution

To confirm that our results are converged with respect to the resolution of the hydrodynamical simulations, we simulated one of the merger simulations (M3M3e) with twice the spatial resolution and 8 times more particles with respect to the standard M3M3e simulation and then performed radiative transfer on the results. Because of both computational constraints and our primary focus being actively star-forming galaxies, we ran this simulation only until slightly after the merger-induced starburst. Figure 10 compares the results of this higher-resolution simulation with those of the standard M3M3e run from L14. The left panel shows the time evolution of the SFR, observed β, and IRX; the solid (dashed) lines correspond to the standard (higher-resolution) M3M3e run. The SFHs of the two simulations differ slightly; consequently, the evolutions of β and IRX differ somewhat. However, the qualitative behavior is identical, and the differences are small. For example, at fixed time, the β values of the two simulations differ by at most 0.3, and the difference is typically $<$0.1. The right panel of Figure 10 compares the evolution of the two simulations in the IRX–β plane; note that the region of the IRX–β plane shown here is much smaller than that shown in the IRX–β plots in the main text because we wish to highlight the (minor) differences between the simulations. Although the detailed evolution of the two simulations differs owing to the different SFHs, the tracks of the two simulations in the IRX–β plane are qualitatively indistinguishable, and the differences

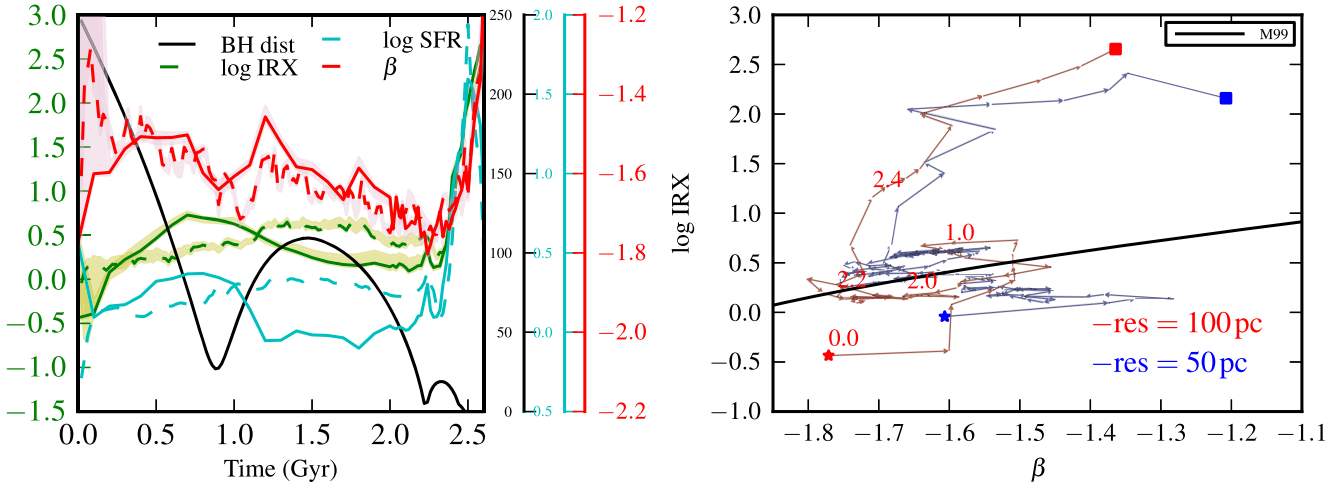

Figure 10. Comparison of the standard M3M3e $z \sim 0$ equal-mass merger with a run with 8 times the number of particles and 2 times smaller softening lengths. Left: time evolution of log IRX, β, log SFR, and supermassive BH separation for both the standard-resolution M3M3e simulation (solid lines) and higher-resolution version (dashed lines). The minor differences in the SFHs of the two simulations result in minor differences in the time evolution of IRX and β, but the qualitative evolution is the same. Right: evolution of the two simulations in the IRX–β plane. Note that the region of the IRX–β plane shown here is much smaller than that shown in the IRX–β plots in the main text because we wish to highlight the (minor) differences between the simulations. The paths of the two simulations differ in detail but are qualitatively identical, and the differences owing to resolution are much less than the uncertainty due to the dust composition.

due to resolution are much less than the uncertainty due to the dust composition (see Section 4).

Appendix B
Effects of Assumptions Regarding Obscuration of Young Stars

The hydrodynamical simulations do not resolve the structure of the ISM on scales $\lesssim$300 pc; this represents one of the primary uncertainties in the radiative transfer calculations (see, e.g., Hayward et al. 2011; Snyder et al. 2013, L14; Hayward & Smith 2015, for detailed discussions). To address this limitation, SUNRISE treats subresolution dust clumpiness using two subresolution models. First, to account for attenuation of young stars by their "birthclouds," the SED templates of Groves et al. (2008) are used when assigning input SEDs to star particles with age <10 Myr. These templates account for dust attenuation, photoionization, and dust reemission in H II regions and PDRs. The time-averaged PDR covering fraction, $f_{\rm PDR}$, is a key parameter that affects the resulting SEDs (see Groves et al. 2008, for details). For our purposes, we note that higher $f_{\rm PDR}$ values result in higher attenuation and thus more dust reemission. The second model accounts for subresolution dust clumpiness outside a star particle's "birthcloud" and is discussed in detail in Appendix C.

Both the $z \sim 0$ and $z \sim$ 2–3 simulations use the Groves et al. (2008) SEDs, but the $f_{\rm PDR}$ values differ: in the $z \sim 0$ simulations, the default value, $f_{\rm PDR} = 0.2$ (Jonsson et al. 2010), is used, whereas in the $z \sim$ 2–3 simulations, $f_{\rm PDR} = 0$ is assumed. Both sets of simulations use the fiducial Jonsson et al. (2010) value for the cluster mass, $M_{\rm cl} = 10^5\ M_\odot$, the other free parameter in the Groves et al. (2008) model. (This parameter has a negligible effect on the results compared with the uncertainties investigated here; see Figure 18 of Jonsson et al. 2010.) The reasons for these choices are discussed in detail in L14 and H13. It is possible that our results are sensitive to both use of the Groves et al. (2008) SEDs (rather than pure STARBURST99 [hereafter SB99] SEDs) and the specific value of $f_{\rm PDR}$ employed. To investigate the former possibility, we reran the radiative transfer calculations for the M3M3e merger simulation using SB99 SEDs for all star particles (rather than the default of Groves et al. 2008 SEDs for <10 Myr old star particles and SB99 SEDs for older star particles). We also reran the M3M3e calculations using the Groves et al. (2008) SEDs for young star particles but assuming $f_{\rm PDR} = 0$ rather than the default value for the $z \sim 0$ simulations, $f_{\rm PDR} = 0.2$. For both of these runs, the $z \sim 0$ default subresolution treatment, "multiphase on" (see the next section), was used. The results of these two runs are compared in Figure 11. The differences between the two are solely due to the effects of the Groves et al. (2008) H II regions because PDRs are not included and the Groves et al. (2008) models use SB99 SEDs as input SEDs.

The left panel of Figure 11 compares the evolution of the two runs in the IRX–β plane. Again, the region shown is a subset of the region shown in the IRX–β plots in the main text because we wish to highlight the differences between the runs. As expected, including the effects of H II regions (the red arrows) results in slightly redder UV slopes. However, the difference in β between the two runs at fixed time is at most $\sim$0.2, which is small compared to that associated with the assumed dust model and comparable to the variation with viewing angle. IRX is essentially unaffected, except for very early times (when IRX is low), and even then, the difference is insignificant for our conclusions.

The right panel of Figure 11 compares the SEDs of the two runs at $t = 2.4$ Gyr. The dashed lines correspond to the input SEDs, whereas the solid lines denote the SEDs that result from the radiative transfer calculations (i.e., they include dust attenuation and reemission from host-galaxy dust). The modest difference in the UV slopes of the input SEDs (the SED that results when the Groves et al. 2008 templates are assumed has a slightly redder UV slope) results in a slight difference in the observed UV slopes. The resulting IR SEDs are almost identical except for the spurious upturn in the SB99 SED at $\sim$200 μm, which has a negligible influence on $L_{\rm IR}$. This is due to a known bug in the version of SB99 employed for this test, and the results presented elsewhere in the paper are unaffected because the Groves et al. (2008) SEDs, which are used for the fiducial runs, do not exhibit this feature. Overall, the this test demonstrates that our results would not change significantly if

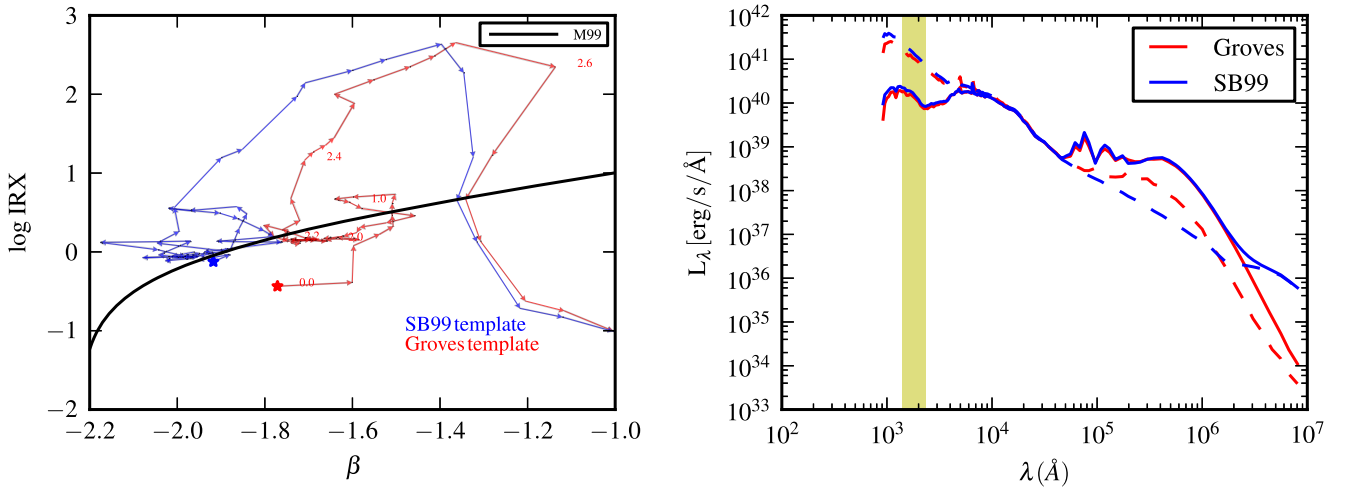

Figure 11. Sensitivity of our results to the use of the H II region model of Groves et al. (2008). In both panels, the red (blue) lines show the results when the effect of H II regions is (is not) included in the radiative transfer calculations; all other assumptions are identical. The left panel shows the IRX–β evolution (note that the β range shown is much smaller than that shown in the IRX–β plots in the main text). Including the effects of H II regions results in slightly redder UV slopes, but the difference in β is small ($\lesssim$0.2). IRX is essentially unaffected, except for very early times. The right panel compares the rest-frame SEDs of the two runs at $t = 2.4$ Gyr. The intrinsic (attenuated) SEDs are indicated by the dashed (solid) lines. The yellow region shows the wavelength range that is used to compute the UV slope. The slight reddening due to H II regions is evident, and it is clear that $L_{\rm IR}$ is unaffected. (N.B. The spurious upturn in the SB99 SEDs at $\sim$200 μm is the result of a known bug in the version of STARBURST99 used only for this test, and it has a negligible effect on $L_{\rm IR}$.) This test shows that our conclusions are insensitive to whether the Groves et al. (2008) H II region model is employed.

we had employed pure SB99 SEDs rather than the Groves et al. (2008) SEDs for <10 Myr old star particles.

To investigate the effect of the subresolution PDR treatment, we compared the fiducial M3M3e run (Groves et al. 2008 SEDs for young star particles, $f_{\rm PDR} = 0.2$, and "multiphase-on" ISM treatment) with the aforementioned run that used the Groves et al. (2008) SEDs and the "multiphase-on" treatment but assumed $f_{\rm PDR} = 0$. The differences between these runs are thus solely due to the attenuation and dust reemission owing to the PDR model. Figure 12 compares the evolution of these two runs in the IRX–β plane. Again, only a small range in β is shown to highlight the differences between the runs. At fixed time, inclusion of PDRs can make the UV slope slightly redder, as expected, but the β values differ negligibly (by <0.1). IRX is noticeably affected only at very early times. This test demonstrates that our results are insensitive to the assumed value of $f_{\rm PDR}$ because in the simulations the attenuation from "resolved" dust (i.e., that directly treated in the radiative transfer calculations) tends to dominate over the attenuation inherent in the Groves et al. (2008) subresolution PDR model (Figure 9 of Jonsson et al. 2010), partially because a significant fraction of the UV luminosity can originate from stars older than 10 Myr, which are attenuated only by diffuse dust. However, it should be noted that assuming an extreme value of $f_{\rm PDR} = 1$ (which we do not advocate; see Hayward et al. 2011) can significantly affect the UV slope (Figure 19 of Jonsson et al. 2010). Moreover, it is possible that the assumptions of the Groves et al. (2008) model regarding, e.g., the birthcloud dispersal timescale do not hold. If so, simply varying the parameters of the model is insufficient to fully explore the uncertainty in the amount of attenuation of UV light from dust on subresolution scales. Ultimately, fully addressing this issue will require performing a similar analysis on ultra-high-resolution hydrodynamical simulations that resolve individual star-forming clouds sufficiently well to directly capture both "local" and "diffuse" dust attenuation of UV light.

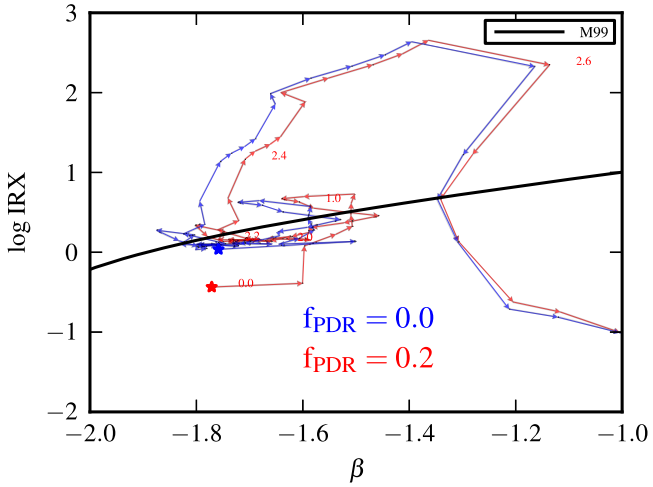

Figure 12. How the IRX–β evolution of the M3M3e major merger depends on the assumed time-averaged PDR covering factor, $f_{\rm PDR}$. The red (blue) arrows show the evolution when the fiducial value $f_{\rm PDR} = 0.2$ ($f_{\rm PDR} = 0$, i.e., no PDRs) is used. All other parameters are identical. Including the effects of PDRs makes the UV slope slightly redder, but the difference in β is small ($\lesssim$0.1). IRX is unchanged except at early times, and the difference then is modest. This test demonstrates that our results are insensitive to whether the effect of PDRs is included in the input SEDs.

Appendix C
Effects of Assumption Regarding the Structure of the ISM on Subresolution Scales

The second subresolution model addresses unresolved dust clumpiness outside of "birthclouds" because the attenuation experienced by a photon packet traversing a given cell can be affected by unresolved clumpiness of the dust within the cell. To characterize the uncertainty associated with this unresolved structure, SUNRISE uses two extreme assumptions. In the first, which has been referred to as "multiphase on" or "default ISM" in previous works, it is assumed that the cold clouds implicit in the Springel & Hernquist (2003) model have zero volume

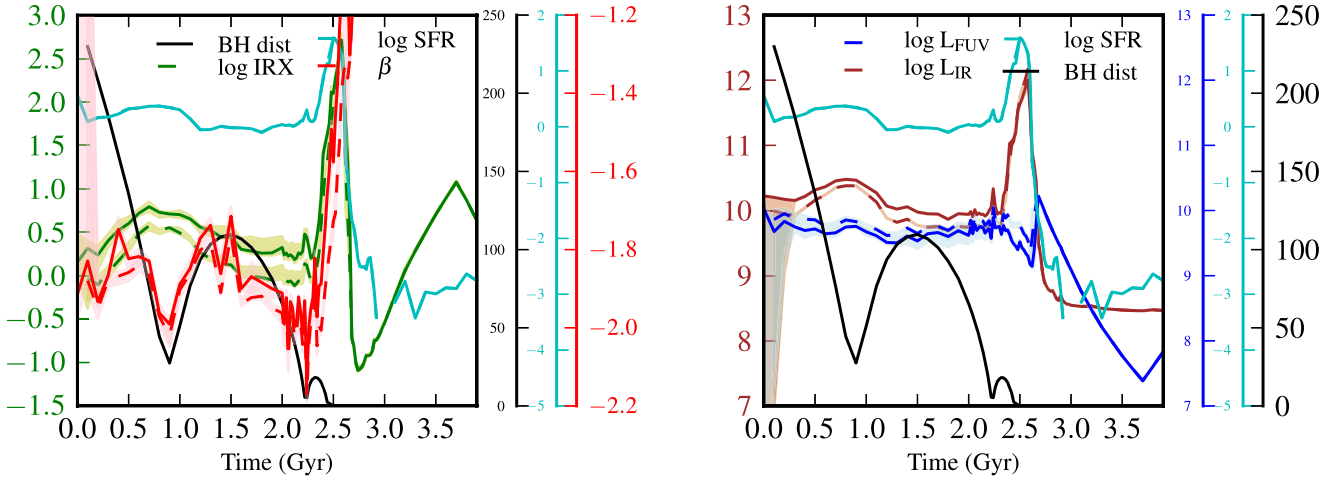

Figure 13. Effects of the treatment of subresolution dust clumpiness. Left: time evolution of IRX and the observed β for the default "multiphase-on" (dashed lines) and "multiphase-off" (solid lines) subresolution ISM models. The SFR and BH separation are also shown for reference. Right: $L_{\rm IR}$, $L_{\rm FUV}$, SFR, and BH separation vs. time; the line styles are the same as in the left panel. Pre-coalescence, using the "multiphase-off" assumption results in slightly higher β, IRX, and $L_{\rm IR}$ and slightly lower $L_{\rm UV}$, as expected (see text), but the differences are minor. Our conclusions are thus insensitive to the treatment of subresolution dust clumpiness that we employ.

filling factor. Thus, the dust content of these clouds is ignored in the radiative transfer calculations. The alternate treatment, which has been referred to as "multiphase off" or "alternate ISM," assumes that the dust density is constant within a given cell. The optical depth of a line of sight through a cell is minimized (maximized) under the multiphase-on (multiphase-off) assumption (e.g., Witt & Gordon 1996).

The default $z \sim 0$ ($z \sim 2$–3) simulations use the "multiphase-on" ("multiphase-off") ISM assumption; see L14 (also Hayward et al. 2011; H13) for justification of these choices. It is possible that our results are sensitive to this assumption. For this reason, we reran the M3M3e radiative transfer calculations using the "multiphase-off" assumption and keeping all other parameters the same as in the fiducial run. The results are compared with the fiducial M3M3e results in Figure 13. The left panel compares the time evolution of the observed β and IRX values (and also shows the SFR and central supermassive BH separation for reference), and the right panel compares the time evolution of $L_{\rm FUV}$ and $L_{\rm IR}$. In both panels, the solid (dashed) lines show the results for the "multiphase-off" (fiducial "multiphase-on") run. Pre-coalescence, using the "multiphase-off" assumption results in slightly higher β, IRX, and $L_{\rm IR}$ values and slightly lower $L_{\rm UV}$ values, as expected given that the "multiphase-off" assumption maximizes the optical depth through a given cell. However, the differences are very small, and our conclusions are thus insensitive to this assumption.

Note that in the right panel of Figure 13, during the starburst induced at merger coalescence, $L_{\rm IR}$ increases sharply because of the elevated SFR, but $L_{\rm FUV}$ decreases because of the increased attenuation experienced by the centrally concentrated starburst. This illustrates why starbursts tend to cause the mergers to move almost vertically in the IRX–β plane and highlights the difficulty of inferring the SFR of highly dust-obscured systems from the UV luminosity: if such systems are contained in a given UV-selected sample, applying a fixed dust correction or using the M99 IRX–β relation will cause the SFR to be significantly underestimated during the starburst. If a significant fraction of the integrated stellar mass is formed in the burst, this underestimate can cause the inferred SFR density to differ significantly from the true value.

References

Agertz, O., & Kravtsov, A. V. 2015, ApJ, 804, 18
Álvarez-Márquez, J., Burgarella, D., Heinis, S., et al. 2016, A&A, 587, A122
Battisti, A. J., Calzetti, D., & Chary, R. R. 2016, ApJ, 818, 13
Bell, E. F., Gordon, K. D., Kennicutt, R. C. J., & Zaritsky, D. 2002, ApJ, 565, 994
Booth, C. M., Agertz, O., Kravtsov, A. V., & Gnedin, N. Y. 2013, ApJL, 777, L16
Boquien, M., Buat, V., Boselli, A., et al. 2012, A&A, 539, A145
Bouwens, R. J., Illingworth, G. D., Franx, M., et al. 2009, ApJ, 705, 936
Bouwens, R. J., Illingworth, G. D., Oesch, P. A., et al. 2012, ApJ, 754, 83
Bouwens, R. J., Illingworth, G. D., Oesch, P. A., et al. 2014, ApJ, 793, 115
Buat, V., Giovannoli, E., Heinis, S., et al. 2011, A&A, 533, A93
Calzetti, D., Kinney, A. L., & Storchi-Bergmann, T. 1994, ApJ, 429, 582
Capak, P. L., Carilli, C., Jones, G., et al. 2015, Natur, 522, 455
Casey, C. M., Scoville, N. Z., Sanders, D. B., et al. 2014, ApJ, 796, 95
Conroy, C., Schiminovich, D., & Blanton, M. R. 2010, ApJ, 718, 184
Cortese, L., Boselli, A., Buat, V., et al. 2006, ApJ, 637, 242
Cox, T. J., Jonsson, P., Somerville, R. S., Primack, J. R., & Dekel, A. 2008, MNRAS, 384, 386
da Cunha, E., Walter, F., Smail, I. R., et al. 2015, ApJ, 806, 110
Dale, D. A., Gil de Paz, A., Gordon, K. D., et al. 2007, ApJ, 655, 863
Draine, B. T., & Li, A. 2007, ApJ, 657, 810
Dunlop, J. S., McLure, R. J., Robertson, B. E., et al. 2012, MNRAS, 420, 901
Dwek, E. 1998, ApJ, 501, 643
Faucher-Giguère, C.-A., Quataert, E., & Hopkins, P. F. 2013, MNRAS, 433, 1970
Finkelstein, S. L., Papovich, C., Salmon, B., et al. 2012, ApJ, 756, 164
Fumagalli, M., Labbe, I., Patel, S. G., et al. 2013, arXiv:1308.4132
Gnedin, N. Y. 2014, MNRAS, 793, 29
Goldader, J. D., Meurer, G., Heckman, T. M., et al. 2002, ApJ, 568, 651
Gordon, K. D., Calzetti, D., & Witt, A. N. 1997, ApJ, 487, 625
Granato, G. L., Lacey, C. G., Silva, L., et al. 2000, ApJ, 542, 710
Grasha, K., Calzetti, D., Andrews, J. E., Lee, J. C., & Dale, D. A. 2013, ApJ, 773, 174
Groves, B., Dopita, M. A., Sutherland, R. S., et al. 2008, ApJS, 176, 438
Groves, B., Krause, O., Sandstrom, K., et al. 2012, MNRAS, 426, 892
Hayward, C. C., Behroozi, P. S., Somerville, R. S., et al. 2013a, MNRAS, 434, 2572
Hayward, C. C., & Hopkins, P. F. 2017, MNRAS, 465, 1682
Hayward, C. C., Jonsson, P., Kereš, D., et al. 2012, MNRAS, 424, 951
Hayward, C. C., Kereš, D., Jonsson, P., et al. 2011, ApJ, 743, 159
Hayward, C. C., Lanz, L., Ashby, M. L. N., et al. 2014, MNRAS, 445, 1598
Hayward, C. C., Narayanan, D., Kereš, D., et al. 2013b, MNRAS, 428, 2529

Hayward, C. C., & Smith, D. J. B. 2015, MNRAS, 446, 1512
Hayward, C. C., Torrey, P., Springel, V., Hernquist, L., & Vogelsberger, M. 2014, MNRAS, 442, 1992
Hopkins, P. F., Kere, D., Oñorbe, J., et al. 2014, MNRAS, 445, 581
Hopkins, P. F., Younger, J. D., Hayward, C. C., Narayanan, D., & Hernquist, L. 2010, MNRAS, 402, 1693
Howell, J. H., Armus, L., Mazzarella, J. M., et al. 2010, ApJ, 715, 572
James, A., Dunne, L., Eales, S., & Edmunds, M. G. 2002, MNRAS, 335, 753
Jonsson, P. 2006, MNRAS, 372, 2
Jonsson, P., Groves, B. A., & Cox, T. J. 2010, MNRAS, 403, 17
Kelson, D. D., & Holden, B. P. 2010, ApJL, 713, L28
Kennicutt, R. C., Armus, L., Bendo, G., et al. 2003, PASP, 115, 928
Khakhaleva-Li, Z., & Gnedin, N. Y. 2016, arXiv:1601.00641
Kong, X., Charlot, S., Brinchmann, J., & Fall, S. M. 2004, MNRAS, 349, 769
Koprowski, M. P., Dunlop, J. S., Michałowski, M. J., et al. 2016, MNRAS, 458, 4321
Kriek, M., & Conroy, C. 2013, ApJL, 775, L16
Lanz, L., Hayward, C. C., Zezas, A., et al. 2014, ApJ, 785, 39
Leroy, A. K., Bigiel, F., de Blok, W. J. G., et al. 2012, AJ, 144, 3
Mao, Y.-W., Kennicutt, R. C. J., Hao, C.-N., Kong, X., & Zhou, X. 2012, ApJ, 757, 52
Mao, Y.-W., Kong, X., & Lin, L. 2014, ApJ, 789, 76
Martínez-Galarza, J. R., Smith, H. A., Lanz, L., et al. 2016, ApJ, 817, 76
McKinnon, R., Torrey, P., & Vogelsberger, M. 2016a, MNRAS, 457, 3775
McKinnon, R., Torrey, P., Vogelsberger, M., Hayward, C. C., & Marinacci, F. 2016b, arXiv:1606.02714
Meurer, G. R., Heckman, T. M., & Calzetti, D. 1999, ApJ, 521, 64
Motta, V., Mediavilla, E., Muñoz, J. A., et al. 2002, ApJ, 574, 719
Muratov, A. L., Keres, D., Faucher-Giguere, C.-A., et al. 2015, arXiv:1501.03155
Narayanan, D., Dey, A., Hayward, C. C., et al. 2010, MNRAS, 407, 1701
Noll, S., Pierini, D., Cimatti, A., et al. 2009, A&A, 499, 69
Oteo, I., Cepa, J., Bongiovanni, A., et al. 2013, A&A, 554, L3
Overzier, R. A., Heckman, T. M., Wang, J., et al. 2011, ApJL, 726, L7
Padin, S. 2014, ApOpt, 53, 4431
Pettini, M., Steidel, C. C., Adelberger, K. L., Dickinson, M., & Giavalisco, M. 2000, ApJ, 528, 96
Reddy, N., Dickinson, M., Elbaz, D., et al. 2012, ApJ, 744, 154
Robertson, B., Hernquist, L., Cox, T. J., et al. 2006, ApJ, 641, 90
Rocha, M., Jonsson, P., Primack, J. R., & Cox, T. J. 2008, MNRAS, 383, 1281
Roebuck, E., Sajina, A., Hayward, C. C., et al. 2016, ApJ, 833, 60
Safarzadeh, M., Ferguson, H. C., Lu, Y., Inami, H., & Somerville, R. S. 2015, ApJ, 798, 91
Safarzadeh, M., Hayward, C. C., Ferguson, H. C., & Somerville, R. S. 2016, ApJ, 818, 62
Salim, S., Dickinson, M., Rich, R. M., et al. 2009, ApJ, 700, 161
Scoville, N., Aussel, H., Brusa, M., et al. 2007, ApJS, 172, 1
Shapley, A. E. 2011, ARA&A, 49, 525
Silva, L., Granato, G. L., Bressan, A., & Danese, L. 1998, ApJ, 509, 103
Smail, I., Swinbank, A. M., Richard, J., et al. 2007, ApJL, 654, L33
Smith, D. J. B., Dunne, L., da Cunha, E., et al. 2012, MNRAS, 427, 703
Snyder, G. F., Cox, T. J., Hayward, C. C., Hernquist, L., & Jonsson, P. 2011, MNRAS, 741, 77
Snyder, G. F., Hayward, C. C., Sajina, A., et al. 2013, ApJ, 768, 168
Sparre, M., Hayward, C. C., Feldmann, R., et al. 2015a, arXiv:1510.03869
Sparre, M., Hayward, C. C., Springel, V., et al. 2015b, MNRAS, 447, 3548
Sparre, M., & Springel, V. 2016, MNRAS, 462, 2418
Springel, V. 2005, MNRAS, 364, 1105
Springel, V., Di Matteo, T., & Hernquist, L. 2005, MNRAS, 361, 776
Springel, V., & Hernquist, L. 2003, MNRAS, 339, 289
Steidel, C. C., Giavalisco, M., Pettini, M., Dickinson, M., & Adelberger, K. L. 1996, ApJL, 462, L17
Takeuchi, T. T., Yuan, F.-T., Ikeyama, A., Murata, K. L., & Inoue, A. K. 2012, ApJ, 755, 144
Utomo, D., Kriek, M., Labbé, I., Conroy, C., & Fumagalli, M. 2014, ApJL, 783, L30
Watson, D., Christensen, L., Knudsen, K. K., et al. 2015, Natur, 519, 327
Witt, A. N., & Gordon, K. D. 1996, ApJ, 463, 681
Wuyts, S., Franx, M., Cox, T. J., et al. 2009, MNRAS, 700, 799
Younger, J. D., Hayward, C. C., Narayanan, D., et al. 2009, MNRAS, 396, L66